Stony Brook University

Characterization of Defects in Single Crystal Epitaxial Silicon for Solar cells

A Thesis Presented

By

Hao Wang

To

The Graduate School

In Partial Fulfillment of the

Requirements

For the Degree of

Master of Science

In

Materials Science and Engineering

Stony Brook University

May 2013

Stony Brook University

The Graduate School

Hao Wang

We, the thesis committee for the above candidate for the

Master of Science degree, hereby recommend

acceptance of this thesis.

Michael Dudley – Thesis Advisor
Professor, Materials Science and Engineering

Balaji Raghothamachar – Second Reader
Assistant Professor, Materials Science and Engineering

T. A. Venkatesh – Third Reader
Assistant Professor, Materials Science and Engineering

This dissertation is accepted by the Graduate School

Charles Taber
Dean of the Graduate School

Abstract of the Thesis

Characterization of Defects in Single Crystal Epitaxial Silicon for Solar cells

by

Hao Wang

Master of Science

in

Materials Science and Engineering

Stony Brook University

2013

In semiconductor technology for solar applications, the demand for high level of structural perfection in single crystal silicon has increased. The defects in the crystals can affect the efficiency of solar cells, so the study of imperfections is important for providing feedback to develop high quality crystal. X-ray topography is a nondestructive method and a powerful tool to evaluate crystals for technological applications, growth and processing.

In this study, defects in homoepitaxial silicon epilayers grown by chemical vapor deposition (CVD) for solar cell application with the dislocation density of $9.4\times 10^{3}cm^{-2}$ have been mapped and characterized by synchrotron white beam X-ray topography (SWBXT), synchrotron monochromated beam X-ray topography, high resolution X-ray diffraction and optical microscopy. In free standing 200μm thick epitaxial single crystal silicon detached from the silicon substrate, a crisscross network of screw dislocations, misfit dislocations and multiple stacking fault configurations are revealed and quantitatively characterized. The silicon epitaxial layer (~60μm) attached to the silicon substrate is characterized by threading dislocations, misfit dislocations and a non-uniform distribution of bending stains from mismatch. These defects can impact the performance and yield of this CVD process for solar cell manufacturing.

Table of Contents

List of Figures v

List of of Abbreviations vi

Acknowledgements iv

Chapter 1 Introduction 1

1.1 Structure of silicon 1

1.2 Background of silicon solar cells 2

1.3 Crystal growth techniques for silicon 4

1.3.1 Czochralski process (CZ) 4

1.3.2 Floating zone (FZ) growth technique 5

1.3.3 Low pressure chemical vapor depostion (LPCVD) 6

1.3.4 Edge defined fed growth technique (EFG) 7

1.3. Ingot technique 7

Chapter 2 Theoretical backgroud 9

2.1 Fundamental of x-ray topography 9

2.2 Diffracted beam intensity 10

2.3 Resolution and contrast formation mechanism in SWBXT 11

2.4 Rocking curve widths (FWHM) 12

2.5 Penetration depth 12

2.6 Fundamental of defects in silicon 13

Chapter 3 Experiment method 16

3.1 Nomarski optical microscopy 16

3.2 Synchrotron White Beam X-ray Topography (SWBXT) 16

3.3 High resolution x-ray diffractometer 18

3.3.1 Doubel axis diffraction 18

3.4 growth method of experimental sample 19

Chapter 4 Results 21

4.1 defects in free-standing 200μm epitaxial single crystal silicon 21

4.1.1 Screw dislocations 21

4.1.2 Misfit dislocations 24

4.1.3 Stacking fault 26

4.2 Defects in 60μm thickness silicon epitaxial with the silicon substrate 29

4.2.1 Threading dislocation 29

4.1.2 Strains in silicon epitaxial 32

Chapter 5 Conclusion 37

References 38

List of Figures

Figure 1.1. (a) Schematic for cubic diamond structure, (b) The distance between two atoms connected by covalent bond is √3/4 a.. 1
Figure 1.2. Atoms in (111) plane projected onto (1-10) with stacking sequence AaBbCc…..... 2
Figure 1.3. Representation of a p-n junction in solar cells illustrating the carrier concentration and formation mechanism for electric field..... 3
Figure 1.4. Schematic of three different silicon structure. (a) structure for single crystal with an infinite periodicity, (b) structure for multicrystalline comprised of many individual grains or crystallites with a local periodicity, (c) structure for amorphous silicon with no long-rang order in the entire crystal..... 3
Figure 1.5. Schematic for CZ processing. 4
Figure 1.6. Processing of silicon wafer production. 5
Figure 1.7. Schematic of a floating zone system 5
Figure 1.8. Schematic of LPCVD processing..... 6
Figure 1.9. Schematic of EDF technique..... 7
Figure 1.10. Schematic description of ingot growth processes.(a) Bridgman technique, (b) HEM (heat extraction) method, (c) EMC technique (electromagnetic casting). 8
Figure 2.1. Three types of geometries for recording topographs. (a) Transmission geometry, (b) Reflection geometries, (c) Back reflection geometry. 10
Figure 2.2. Schematic of the mechanism of orientation contrast..... 11
Figure 2.3. Schematic ray diagram for calculation of penetration depth 12
Figure 2.4. (a) (b) Thompson tetrahedron model. (c) Planar representation of the Thompson tetrahedron. 16
Figure 3.1. (a) Schematic of transmission x-ray topography technique, (b)Transmission topographs with different g vector 220, 33-1, -11-1 and 0-40..... 17
Figure 3.2. Schematic of reflection geometry x-ray topography technique..... 18
Figure 3.3. Double axis x-ray diffractometer..... 19
Figure 4.1. Defects in free-standing 200μm epitaxial single crystal silicon shown in 1-1-1 reflection..... 21
Figure 4.2. Transmission topographs used for burgers vector analysis with g vector (1-1-1), (220), (-220), (33-1)..... 22
Figure 4.3. High magnification topographs from selected region of different reflections. Some inclusions are observed in these images. (a) 1-1-1; (b) 220; (c) -220; (d) 33-1..... 23
Figure 4.4. (a) Magnification image with area contains misfit dislocations in -11-1 reflection. (b), (c), (d) illustrate the mechanism for formation of misfit dislocations with burgers vector 1/2[110], which has been analyzed in 4.1.1, and the it is screw dislocation..... 24
Figure 4.5. (a) Magnification image contains half-loop like misfit dislocation in -11-1 reflection, (b) Formation mechanism of half-loop like dislocation..... 25

Figure4.6. (a) Transmission topography of 1-11 reflection; (b) the pyramid structure, up four faces are formed by (111) and bottom face a (001); (c) square feature in 1-11 reflection; (d) square feature in 2-20 reflection; (e) square feature in 040 reflection. 27
Figure 4.7. Images from optical microscopy on surface plane (001) in BF mode shows mechanical formation of stacking fault. 28
Figure 4.8. The triangle dark feature is invisible in (a) and visible in (b) and (c), the reflection of these three topography are separately 1-1-1, 1-11, -220. 28
Figure 4.9. Reflection topography (g = 040) of 60μm thickness silicon epitaxial with the silicon substrate29
Figure 4.10. Schematic showing the experimental setting-ups at APS..... 30
Figure 4.11. Reflection topography from APS with 040 reflection. (a) image from middle section of the sample, (B) magnification images from the area of the white square in (a).. 31
Figure 4.12. Illustration for the formation of TD..... 31
Figure 4.13. Diamond shape misfit dislocations represented in the magnification image. 31
Figure 4.14. Transmission topograph shows strain area and strain free area.. 32
Figure 4.15. (a) The geometry for section topography, the transmitted diffraction image from a restricted region is recorded, (b) section topograph from high strain area.. 33
Figure 4.16. Image for one of the rocking curve recorded..... 34
Figure 4.17. 121 positions recorded on the sample..... 34
Figure 4.18. 3-D model for FWHM distribution, X axis stands for horizontal length of this sample, and Y axis stands for the vertical length of this sample and Z axis stands for the FWHM value... 35

List of Abbreviations

CZ: Czochralski process
FZ: Floating zone
LPCVD: Low pressure chemical vapor deposition
PECVD: Plasma-enhanced chemical vapor deposition
EFG: Edge defined fed growth
HEM: Heat extraction method
EMC: Electromagnetic casting
SWBXT: Synchrotron white beam x-ray topography
FWHM: Full width at half maxima
XRD: X-ray topography
TD: Threading dislocation

Acknowledgements

First I would like to give my sincere gratitude to Prof. Michael Dudley, for giving me an opportunity to work in the crystal characterization field. I also want to give my sincere appreciation to Dr. Balaji Raghothamachar for his wide knowledge, helpful guidance and encouragement during my graduate studies. Without a doubt, both Prof. Dudley and Dr. Raghothamachar have assisted me in landing a great post-graduate career opportunity.

Second, I would like to thank my parents for their strong support throughout my graduate study, without them, I would not have been able to complete my graduate studies.

Thanks are also given to Prof. T. A. Venkatesh for being my dissertation committee members and his valuable advice.

I would also want to thank my colleagues: Ms. HuanHuan Wang, Mr. Fangzhen Wu, Mr. Shayan Byrappa, and Ms. Shun Sun for their valuable support and help during my research.

Topography experiments were carried out at the Stony Brook Synchrotron Topography Facility, BNL, at Beamline X-19C and at Beamline1-BM at APS, ANL. The NSLS is supported by the Department of Energy under Contract DE-AC02-76CH00016.The APS is supported by the U.S. Department of Energy, Office of Science, Office of Basic Energy Sciences, under Contract No. DE-AC02-06CH11357.

Chapter 1 Introduction

1.1 Structure of silicon

Silicon crystallizes in the diamond cubic crystal structure (space group Fd3m) as shown in figure 1.1.(a), the lattice constant is a=0.543nm. The Bravais lattice is face-centred cubic with another four atoms inside the cubic, the coordinates of these four atoms can be taken to be (1/4,1/4,1/4), (3/4,3/4,1/4), (3/4,1/4,3/4), (1/4,3/4,3/4) which occupy the position of four tetrahedral interstitial spaces in face-centred cell. The coordination number is four, with the nearest neighbors at a distance $\frac{\sqrt{3}}{4}a$ as shown in figure1.1.(b).

In diamond structure, the close-packed plane is {111} which is the same as in face-centred cubic, the stacking of (111) plane in the diamond structure is shown in figure 1.2. The atomic positions are projected onto $(1\,\bar{1}\,0)$, the stacking sequence of successive (111) planes are AaBbCcAaBbCc. The glide plane is the close-packed plane {111} and the Burgers vector of perfect dislocation is $\frac{1}{2}$<110>, dislocations tend to lie along <110> direction as this direction has a low dislocation energy, therefore, two types of perfect dislocations in diamond lattice are the screw dislocation and the so called 60^0 dislocation, where the Burgers vector is inclined at the angle of 60^0 to the dislocation line.

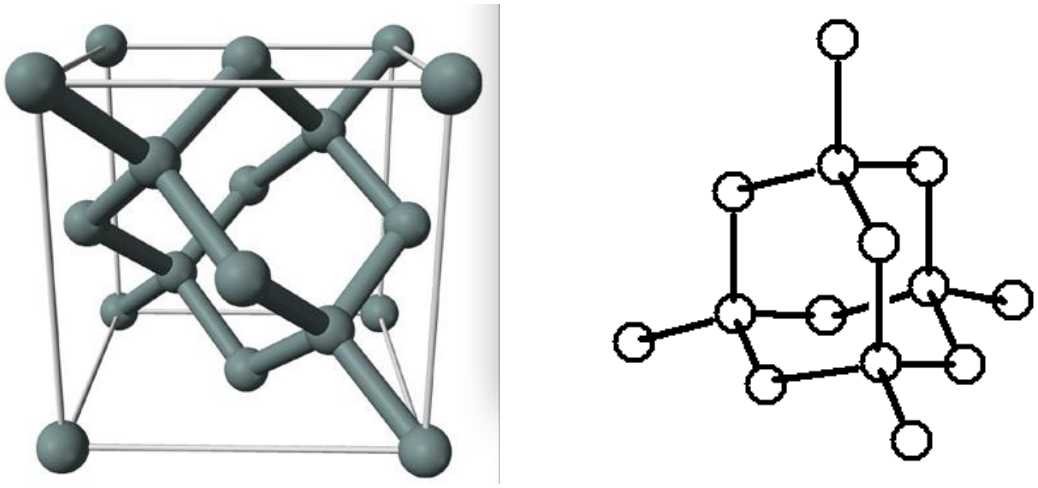

Figure 1.1. (a) Schematic for cubic diamond structure, (b) The distance between two atoms connected by covalent bond is $\frac{\sqrt{3}}{4}a$.

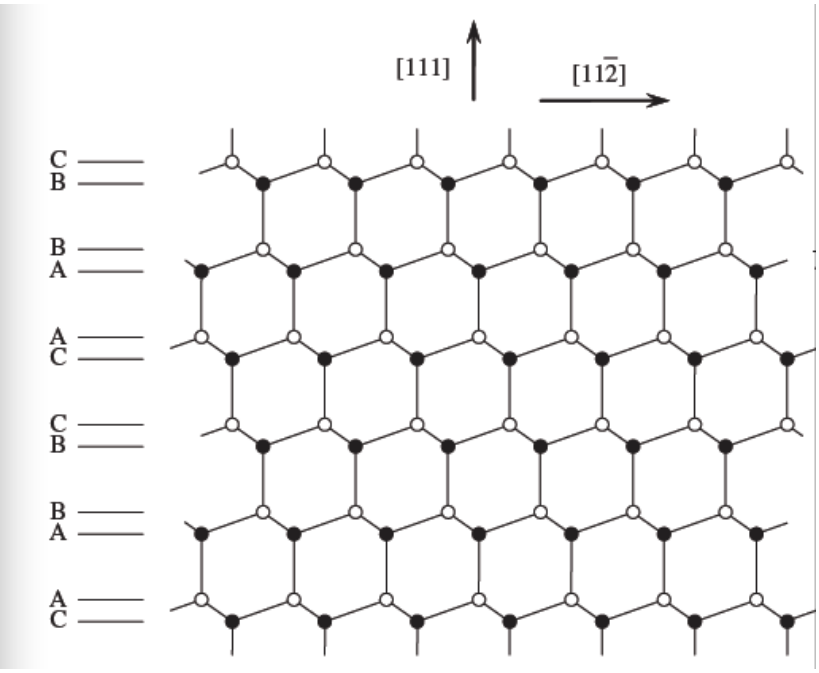

Figure 1.2. Atoms in (111) plane projected onto (1-10) with stacking sequence AaBbCc…

1.2 Background of silicon solar cells

In the production of solar cells based on semiconductor materials, silicon is the ideal material so far. The principle of solar cells is the photovoltaic effect, which means the electrical device converts energy of light directly into electricity.

The electrical field is created by the p-n junction (figure 1.3), which is made from silicon. A piece of n-type silicon is doped with phosphorous, having five valence electrons, so the concentration of electrons in this region is much higher than that of holes. While a piece of p-type silicon is doped with boron, which has three valence electrons, which has a much higher concentration of holes. When the two different type of pieces contact with each other, the charge carriers diffuse from high concentration to low concentration creating an electric field from n-type region towards p-type region, the electric field is responsible for separating the newly generated electron-hole pairs from recombining when light in incident on the solar cells [1]. When p-n junction connects with an external circuit, the photo current are equal with the current in the external circuit, which can produce a stable electric potential difference V_{oc} in the two ends of p-n junction. In this case, p-n junction has played a role as power supply, as long as the light does not stop, there will be a continuous electrical current through the circuit. This is the basic principle of the solar cell.

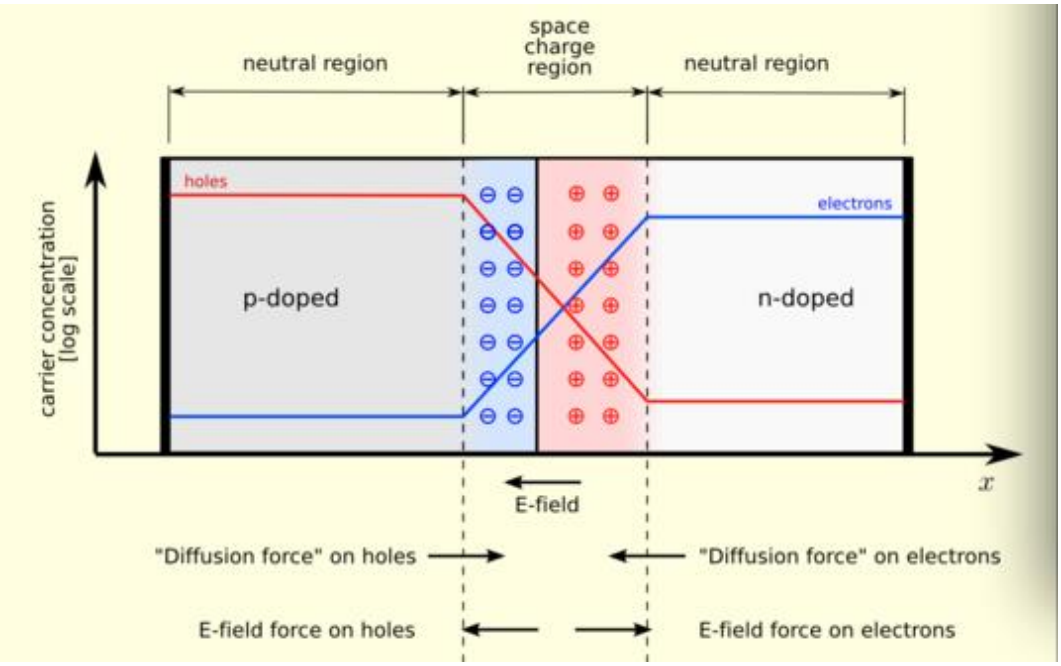

Figure 1.3. Representation of a p-n junction in solar cells illustrating the carrier concentration and formation mechanism for electric field. [2]

The main motivations for solar cell research and development are to increase the conversion efficiency and decrease in cost. Silicon used for photovoltaic solar cells can be divided into three types: single crystal silicon, multicrystallline silicon (mc-Si), and amorphous silicon (a-Si). Single crystal silicon (c-Si) is the most popular of the three types. It has the highest efficiency, and has been studied widely for decades. The growth methods for single crystal silicon are Czochralski process and floating zone method. The wafer of single crystal silicon is expensive, due to lost as sawdust (~20%) during dicing from cylindrical ingots and waste of material by refining the square solar cell module [3].

On the other hand, multicrystalline and amorphous silicon cells have low cost because they do not require dicing during production. Despite their low cost, these two types of silicon solar cells have low efficiency, making them less advantageous. Current efficiency achieved in laboratory for single crystal, multicrystalline, and amorphous silicon solar cells are respectively 25%, 20.4%, 12.5% [4]. Steabler-Wronski effect is the reason for low conversion efficiency in amorphous silicon cells [5]. The most popular method for multicrystalline silicon is ingot casting while for amorphous silicon production usually uses PECVD method.

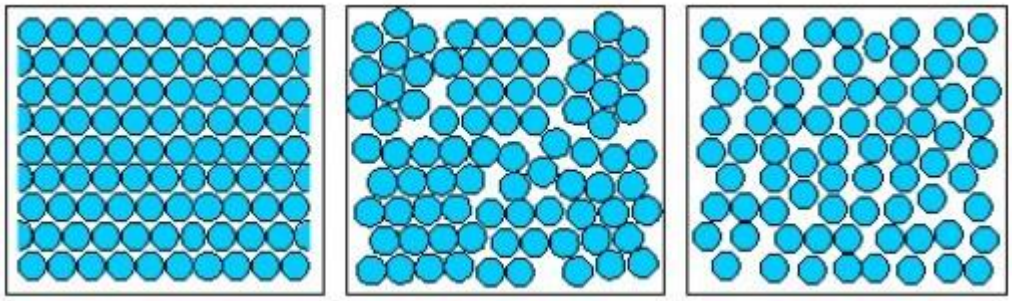

(a) (b) (c)

Figure 1.4. Schematic of three different silicon structure. (a) structure for single crystal with an infinite periodicity, (b) structure for multicrystalline comprised of many individual grains or crystallites with a local periodicity, (c) structure for amorphous silicon with no long-rang order in the entire crystal. [6]

1.3 Crystal growth techniques for silicon

1.3.1 Czochralski (CZ) process

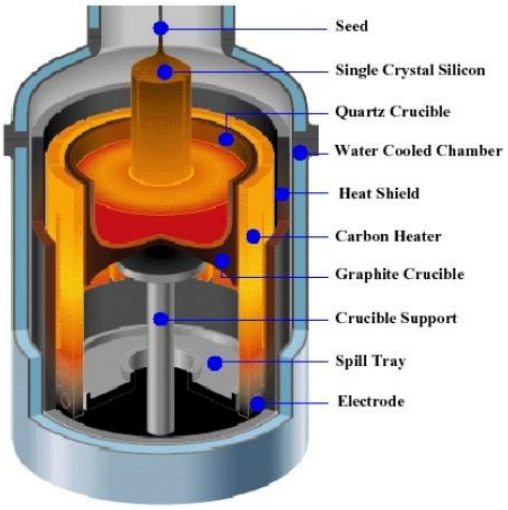

Figure 1.5. Schematic for CZ processing [7]

CZ is more common method for growth of large cylindrical ingots, or boules, of single crystal silicon. High quality silicon is melted down in the quartz crucible, dopant such as boron and phosphorous can be added into the molten silicon in order to change it to n-type or p-type silicon. The seed crystal with specific orientation is mounted on a rod and dipped into the molten silicon; the rod is pulled upwards and rotated slowly at the same time. Large

cylindrical ingots size and high quality can be extracted by controlling the temperature gradient, rate of pulling (1mm/min) and speed of rotation.

In order to avoid the contamination during CZ process, it should be performed under the inert atmosphere, but impurity such as oxygen still can be incorporated into the melt, which comes from the dissolution of crucible walls. While the oxygen impurities have beneficial effect, it can improve the mechanical strength of silicon wafer by immobilizing the dislocations which may be introduced during device processing [8] [9].

Nowadays, the largest silicon wafer can be produced is 400mm in diameter, and the standard industry diameter of wafer are 200mm and 300mm. In order to get thin, high flatness silicon wafer (usually ~0.75mm), dicing, grinding, chamfering and polishing is also needed, figure1.6 illustrates the processing of silicon wafer.

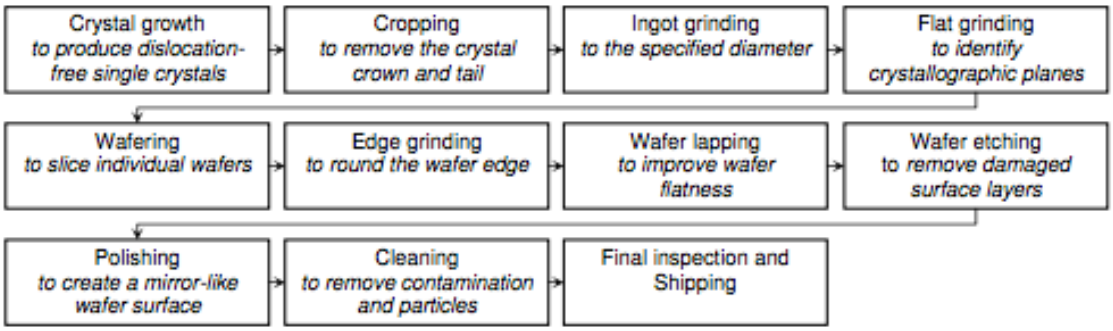

Figure 1.6. Processing of silicon wafer production

1.3.2 Floating zone (FZ) growth technique

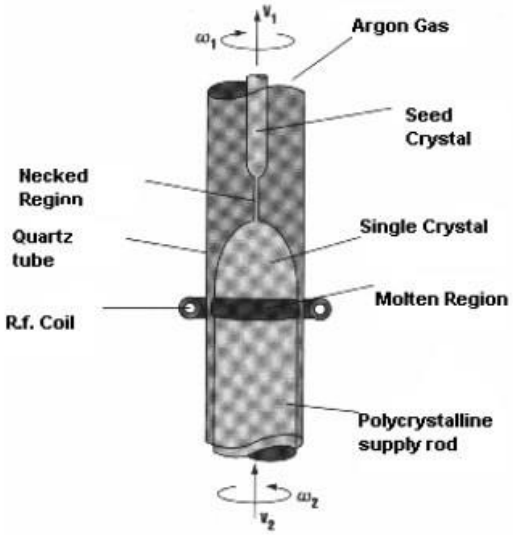

Figure 1.7. Schematic of a floating zone system [10]

CZ silicon wafers are contaminated by oxygen and carbon from the crucible, so the CZ silicon wafers have relatively low purity. While FZ growth technique is a method to get extremely high purity silicon due to there is no need for a crucible. Figure1.7 illustrates the floating zone growth method, high purity polycrystalline rod is held in a chuck and the molten part of polycrystalline rod is supported by the solid part under the Argon gas atmosphere. A metal coil which can produce heat stands around the purity polycrystalline material and moving slowly from up to down, meanwhile, the molten silicon at the silicon crystal seed end starts to freeze. After the metal coil move over the whole polycrystalline rod, it converts to single crystal silicon which has the same
crystal orientation with the crystal silicon seed.

This technique was developed by Henry Theuerer at Bell Labs in 1955 [11]. Due to the surface tension limitations during growth, this method can only produce the radius of the single silicon ingot not greater than 150mm. The light impurities, such as carbon and oxygen can be controlled in extremely low level, but another impurity, nitrogen is being intentionally added during growth processing as it can reduce the microdefects and improve the mechanical strength of the silicon wafers [12].

1.3.3 Low pressure chemical vapor deposition

LPCVD is a common growth method in deposition of multicrystalline silicon and is similar to other types of CVD technique that it is a process where a gas species reacts on the substrate and the reaction produces a solid material; the gaseous species used for reaction are silane ($SiHCL_3$) or trichlorosilane ($Si H_4$). As the name of this method, it required lower pressure which can be from 0.1 to 2 torr, and the deposition temperature is relatively higher which is from 600 to 650° . The process occurs in a quartz tube, when the tube is heated to the desired temperature, the gas species is inserted into the tube and reacts with the substrate and create a solid phase material. The temperature of the substrate is very important and it can influence what kind of reactions will take place. Finally, the excess gases will be pumped out of the tube. The following reactions are usually performed in LPCVD systems [13]:

$SiHCl_3 \rightarrow Si + H_2 + HCl$

$SiH_4 \rightarrow Si + 2H_2$

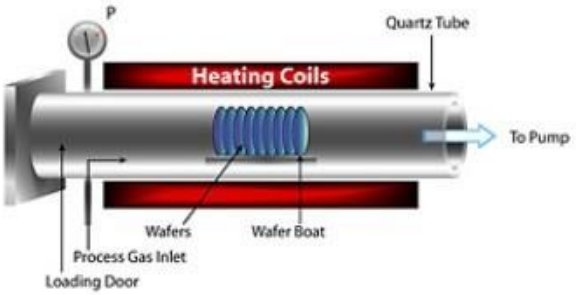

Figure1.8. Schematic of LPCVD processing [14]

Comparing to other CVD methods, the advantages of LPCVD are high purity, uniformity of thickness and homogeneous deposited lays, but this process requires high temperature and the deposition rate is lower.

1.3.4 Edge defined fed growth technique (EFG)

Another commercial growth technique for multicrystalline silicon production is Edge Defined Fed Growth Technique (EFG), it is one of the Ribbon techniques. EFG was invented by H.Labelle in 1960s [15]. Figure1.9 is the schematic for EFG system. Desired sectional shape can be obtained in the form of ribbons, tubes, rods and others based on the shaping system. Using of a ring channel, capillary feeding was achieved; the silicon melt was raised by capillary to the top of the orifice. The silicon melt is then touched by the seed crystal at proper melting temperature, while the seed crystal is slowly pulled from the molten silicon and the final crystal is grown. Main advantages of the EFG method are growth of near net shape which domains zero or small need of machining decreasing production costs, possibility of growth of complicated shapes and large scale profiles, higher growth rate and also automated process control. The growth rate is equal to the crystalline rate which is about 1cm/min. In order to achieve high growth rate, temperature gradients of more than 200k/cm have to be used at the silicon melt interface, lead to large thermal stresses, grain boundaries in growth direction and high density of dislocations [16] [17].

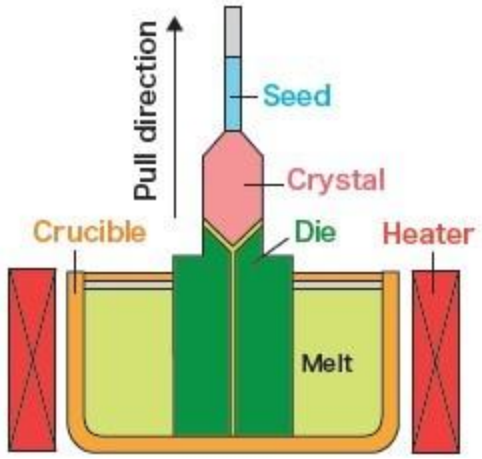

Figure 1.9. Schematic of EDF technique

1.3.5 Ingot technique

The main methods of ingot technique for multicrystalline silicon growing are illustrated in figure 1.10. Bridgeman technique consists of filling the high purity molten silicon or

pouring the molten silicon inside the crystallization crucible, the crystallization and cooling processes then take about 30 to 40 hours. Heat extraction method (HEM) is a modification of the Bridgeman technique, which can extract the heat locally at the bottom of the crucible. Crystals were produced from both of the techniques can contain impurities due to the contact of the melt and the crystals with the crucible walls as in CZ method. The mainly impurities are SiO2 from crucible walls, Si3N4 from coating layer and graphite from the support die, which can segregate along the growth direction and formation of precipitates and determine the final quality of the crystal. The electromagnetic casting (EMC) technique is processing without crucible, so the impurities can be avoided but at the cost of higher stresses and dislocation densities. None of these techniques is a good choice for crystals or solar cells production due to the relatively low crystal quality [18] [19].

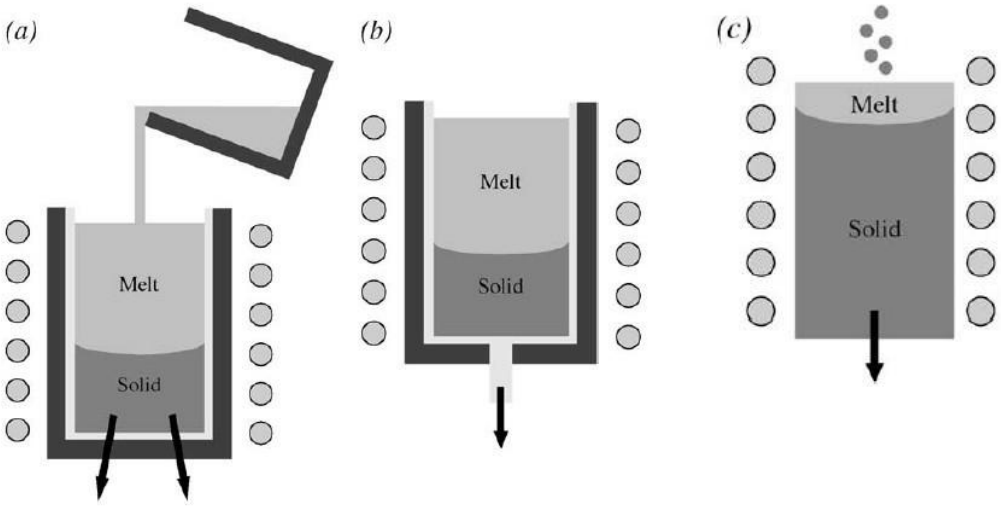

Figure 1.10. Schematic description of ingot growth processes.(a) Bridgman technique, (b) HEM (heat extraction) method, (c) EMC technique (electromagnetic casting).

Chapter 2 Theoretical background

2.1 Fundamentals of x-ray topography

X-ray topography is a non-destructive technique widely used for evaluating crystal quality and visualizing defects in many different low defect density crystalline materials ($<10^{-6}/cm^2$). X-ray beam is generated by X-ray tube or a synchrotron source, the latter with the advantages of high intensity, lower divergence and continuous wavelength spectrum makes it to be a good candidate. X-ray topography is based on the kinematical and dynamical diffraction of x-ray beams with crystal lattices. The kinematical theory is useful when x-ray interacts with a relatively small crystal, and in this theory assumes that x-ray is scattered by atoms in the small crystal only once and the loss of re-scattering intensity is negligible. While for perfect crystals, the dynamical theory is a good approximation, multiple scattering occurs when x-ray interacting with a perfect crystal. The images record the intensity of the beam diffracted by a set of lattice planes (hkl) of a crystal, thus as the condition satisfy the Bragg law, the X-ray diffraction can occur.

$\lambda = 2d_{hkl}\mathrm{Sin}\theta$

In the Bragg equation, where λ is the wavelength of the X-rays, d_{hkl} is interplaner spacing and θ is the angle between incident beam and lattice plane. The diffracted intensity of the x-ray beam is given by equation according to the kinematical theory.

In x-ray topography, the images are formed from the diffracted beam when x-ray beam is incident on thesample, the two dimensional detector usually used to record the images are high-resolution x-ray film, CCD detector or a nuclear plate. The images for perfect crystals usually have a homogeneous contrast, but contrast changes in images from the imperfect crystals is caused by deviations, from perfect long-range atomic order. X-ray topography has its roots in the classical laboratory x-ray work of the 1930s through the 1960s [20], the technique is developed by using characteristic x-rays from laboratory source, and the development of synchrotron radiation sources has enabled white beam topography and monochromatic x-ray topography techniques possible. In practice, x-ray topograph can be created in many ways; some classical fundamental topographic techniques are listed below:

(1). Section topography
(2). Berg-Barrett method
(3). Double crystal topography
(4). White beam topography [x-ray topography]

White beam topography is the topographic technique method we use in our study; we have used three types of geometries for recording topographs (Figure 2.1): (1) Transmission geometry, (2) Reflection geometries, and (3) Back reflection geometry. We will explain the detail about these geometries in the following section.

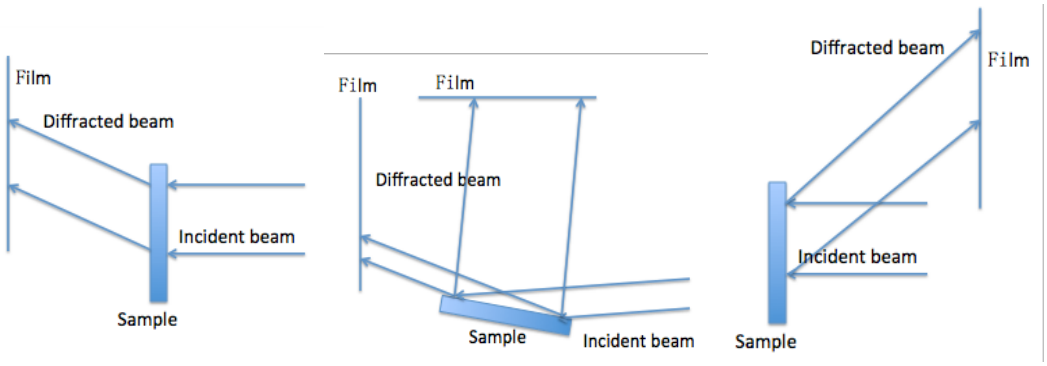

Figure 2.1. Three types of geometries for recording topographs. (a) Transmission geometry, (b) Reflection geometries, (c) Back reflection geometry.

2.2 Diffracted beam intensity

The diffracted intensity is proportional to the square of the magnitude of the structure factor according to equation shows below. If absorption is ignored, the rocking curve widths is also related to the structure factor, thus, the structure factor is an important parameter in our experiments, the structure factor F_{hkl} is defined as:

$$F_{hkl} = \sum_i f_i \exp\{-2\pi i(Hx_i+Ky_i+Lz_i)\}$$

Where f_i is the atomic scattering factor, (xyz) is the coordinates of the atoms in the unit cell, (HKL) is the miller index of the reflection plane. The structure of Silicon is diamond cubic structure, which has eight atoms in one unit cell, the coordinates of silicon atoms in the unit cell are:

(0, 0, 0) (1/4, 1/4, 1/4) (0, 1/2, 1/2) (1/4, 3/4, 3/4)

(1/2, 0, 1/2) (3/4, 1/4, 3/4) (1/2, 1/2, 0) (3/4, 3/4, 1/4)

Based on Eulre equation, equation can be written as Trigonometric functions:

$$F_{hkl} = \sum_i f_i[\cos 2\pi(Hx_i+Ky_i+Lz_i)+i\sin 2\pi(Hx_i+Ky_i+Lz_i)]$$

Therefore the structure factor can be written as:

$$F_{hkl} = f_{si}[e^{-2\pi i(\frac{1}{2}K+\frac{1}{2}L)}+e^{-2\pi i(\frac{1}{2}H+\frac{1}{2}L)}+e^{-2\pi i(\frac{1}{2}H+\frac{1}{2}K)}+e^{-2\pi i(\frac{1}{4}H+\frac{1}{4}K+\frac{1}{4}L)}+e^{-2\pi i(\frac{1}{4}H+\frac{3}{4}K+\frac{3}{4}L)}+ e^{-2\pi i(\frac{3}{4}H+\frac{1}{4}K+\frac{1}{4}L)}+e^{-2\pi i(\frac{3}{4}H+\frac{3}{4}K+\frac{1}{4}L)}]$$

After some calculation, the relationship between Miller index and diffracted intensity is shown below:

1) When H, K, L are odd:

$$F_{hkl}^2 = 32 f_{si}^2$$

$F_{hkl} = 4\sqrt{2}f_{si}$

2) When H, K, L are even and H+K+L=4n:

$F_{hkl}^2 = 64f_{si}^2$

$F_{hkl} = 8f_{si}$

3) When H, K, L are mixed or H, K, L are even and H+K+L≠4n:

$F_{hkl}^2 = 0$

$F_{hkl} = 0$

2.3 Resolution and contrast formation mechanism in SWBXT

High resolution can be achieved using x-ray source from synchrotron radiation due to high intensity, lower divergence and small source dimensions. The topographic resolution(R) can be given by equation [21], where S is source dimension perpendicular to the plane of incidence, D is the distance between source and specimen, and d is the specimen film distance. The theoretical spatial resolution we use in Beamline X19C at NSLS of Brookhaven National Laboratory is 0.4 um.

$$R = d\ S/D$$

Complex interaction between crystal lattice and x-rays can give rise to topographic contrast, thus interpreting x-ray topographic contrast of defects is complicated. Generally speaking, there are two basic mechanisms for contrast in x-ray topographs: orientation contrast and extinction contrast.

Orientation contrast arises from non-uniform diffracted x-ray intensity distributions, regions of different orientation (grains, boundaries, twins) arising overlap or separation (figure) of diffracted x-rays in varying directions. In the white beam XRT, the misorientated region choose the wavelength to satisfy the Bragg law, the orientation contrast appears to be white due to the divergence of diffracted x-ray beams and to be dark due to the convergence of x-ray beams.

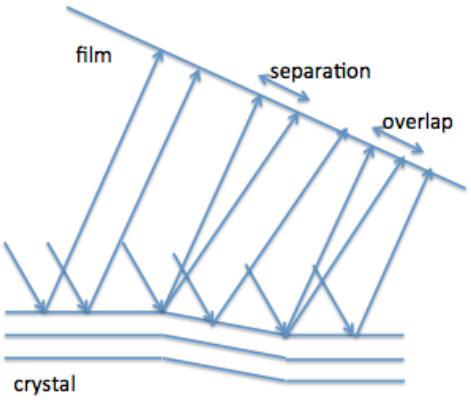

Figure 2.2. Schematic of the mechanism of orientation contrast

Extinction contrast arises when the scattering power in the defects is different from other regions in the crystal; understanding of dynamical diffraction in highly perfect crystal is useful to interpret this contrast. Three types of extinction contrast produce contrast of dislocations in topography: direct image contrast, dynamic contrast and intermediary contrast. In transmission geometry, the contrast types of images can be determined by the absorption condition (μt), absorption condition is the product of linear absorption coefficient u and the thickness of crystal t.

Direct dislocation image: This type of image is observed under absorption condition μt<1, diffracted intensity is higher in dislocation core region than the surrounding matrix, dark dislocation lines appears in this case.

Dynamical dislocation image: This type of image appears under absorption condition μt>6, Borrmann effect gives rise to white dislocation lines.

Intermediary dislocation image: This type of image is observed under absorption condition 1< μt < 6, all of the three contrast mechanisms can give a contribution to this type of image [22].

2.4 Rocking curve widths (FWHM)

Rocking curve widths is defined by x-ray diffracted intensity versus angle curve, in Bragg case, the FWHM is given by [23]:

$$2\delta = \frac{2r_e \lambda^2}{\pi V sin2\theta} \frac{1}{\sqrt{|\gamma|}} |C||F_{HKL}|$$

and in Laue case, it is given by:

$$2\delta = \frac{2r_e \lambda^2}{\pi V sin2\theta} \sqrt{|\gamma|}|C||F_{HKL}|$$

Where r_e is the radius of electron, λ is the wavelength of x-ray, V is the volume of unit cell, θ is the bragg angle, γ is the asymmetric ratio, C is the polarization factor and F_{HKL} is the structure factor. FWHM is a critical parameter to determine the crystal quality, the narrower the FWHM, the better the crystal quality. Dislocations, grain boundaries and strain can broaden the rocking curve. In addition, extinction contrast is related to rocking curve widths, the width of dislocation on the image is raised by the kinematical diffracted region near the dislocation core, which is determined by the rocking curve width.

2.5 Penetration depth

The penetration depth is an important parameter in x-ray topography study. It can provide the information about depth of the samples recorded in the film. The penetration depth can be raised by kinematical penetration depth or by dynamical penetration depth. The kinematical penetration is given by [24]:

$$t = \frac{1}{\mu(\text{cosec}\alpha + \text{cosec}\beta)}$$

Where μ is the mass absorption coefficient, α *and* β are the angles of the incident and diffracted beams with respect to surface, respectively. The schematic of penetration depth geometry is shown in figure 2.3.

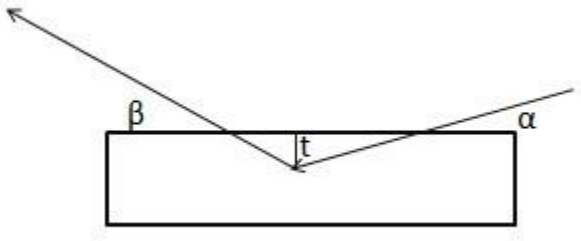

Figure 2.3. Schematic ray diagram for calculation of penetration depth

However, for nearly perfect crystals, the penetration depth in Bragg geometry is governed by extinction distance. According to the dynamical theory, the penetration depth is thus given by [25]:

$$Z_e = \frac{\lambda\sqrt{|\gamma_h\gamma_o|}}{\frac{2\pi r_e\lambda^2}{\pi V}\sqrt{F_h F_{\bar{h}}}\sqrt{1-\eta^2}}$$

Where λ is the wavelength, γ_h=cosψ_h (ψ_h is the angle between the diffracted beams with surface normal), γ_0=cosψ_0 (ψ_0 is the angle between the incident beams with surface normal), C is the polarization factor, r_e is the classical radius of electrons, V is the volume of the unit cell, η is the deviation parameter (the deviation from the rocking curve peak).

Since the samples we studied have relatively high dislocation density (~$10^4$to $10^6/cm^2$), the kinematical penetration is dominated and determines the penetration depth in the x-ray diffraction.

2.6 Fundamentals of defects in silicon

The defects in silicon have been widely studied so far, and these defects are generally divided by the dimension:

1) 0-D (zero-dimension) defect (point defect): include intrinsic interstitial atoms, vacancies and substitution impurities.
2) 1-D defect (linear defect): dislocations, such as edge dislocations, screw dislocations and misfit dislocations;
3) 2-D defect (planar defect): stacking faults, grain boundaries and twins;

As mentioned in chapter 1, silicon has a diamond cubic structure; the closed packed plane and direction in this structure separately are {111} and <011>. Most of the dislocation lines tend along <011> direction and 60° angle to the Burgers vector. In addition, Burgers vector for perfect dislocations in silicon is ½<011> [26].

Thompson's tetrahedron is a convenient model to describe all the dislocations in the diamond facial centre cubic structure. As shown in figure 2.4(a) and (b), a set of four {111} planes are parallel to the four face of the tetrahedron and the <011> slip directions are parallel to the edges of tetrahedron. A, B, C, D are in the corner of the tetrahedron and α, β, γ, δ are in the middle of each face.

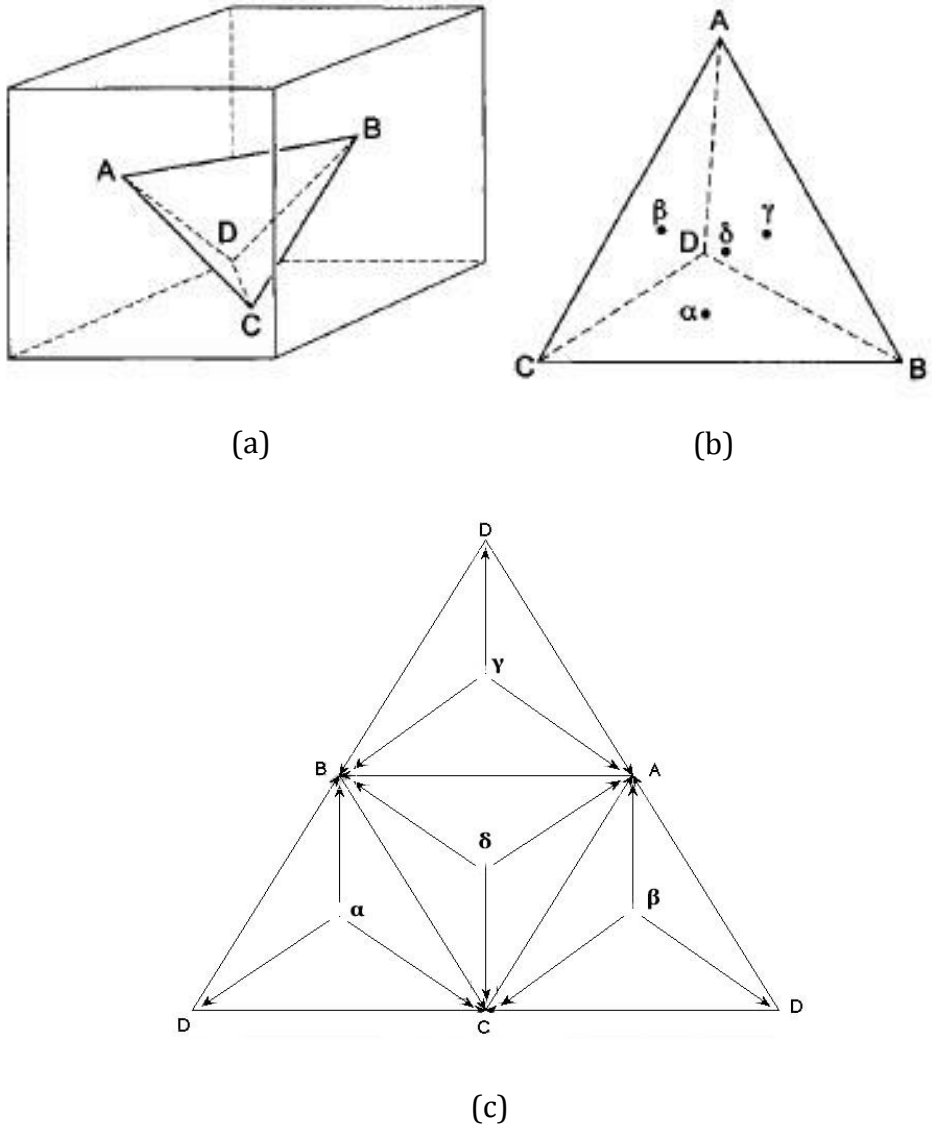

Figure 2.4. (a) and (b) are the Thompson tetrahedron model. (c) Planar representation of the Thompson tetrahedron.

The Burgers vectors and the possible reactions in the Thompson's tetrahedron are presented below:

DA = 1/2[011], DB = 1/2[101], DC = 1/2[110], AB = 1/2[$1\bar{1}0$], BC = 1/2[$01\bar{1}$],CA = 1/2[$\bar{1}01$];

Dδ = 1/3[111], Cγ = 1/3[$\bar{1}\ \bar{1}1$], Bβ = 1/3[$\bar{1}\ \bar{1}\ \bar{1}$], Aα = 1/3[$1\bar{1}\ \bar{1}$];

αB = 1/6[$1\bar{1}2$], αC = 1/6[$12\bar{1}$], αD = 1/6[$\bar{2}1\bar{1}$], δA = 1/6[$\bar{2}11$], δB = 1/6[$1\bar{2}1$],

δC = 1/6[$11\bar{2}$], γA = 1/6[$\bar{1}21$], γB = 1/6[$2\bar{1}\ \bar{1}$], γD = 1/6[$11\bar{2}$], βA = 1/6[$\bar{1}12$], βC = 1/6[$21\bar{1}$],

βD = 1/6[$\bar{1}\ \bar{2}\ \bar{1}$].

δA = DA –Dδ

δB = DB – Dδ

δC = DC - Dδ

Chapter 3 Experiment method

In this study, the combined use of Nomarski optical microscopy, SWBXT and high Resolution X-ray Diffractometer has been employed for characterization of defects structures in epitaxial silicon (~60μm) on substrate (~720μm) and free-standing silicon (~200μm).

3.1 Nomarski Optical Microscopy

Nomarski optical microscopy (Nikon Eclipse E600 POL) is used for examining surface morphology of crystals, comparing with x-ray topographs and separating contrast features on crystal surface by processing or polishing (scratch) from contrast features caused by lattice defects. Using optical microscopy, crystallographic information of growth facets and steps can be determined from the single crystal surface.

3.2 Synchrotron White Beam X-ray Topography (SWBXT)

SWBXT experiments were performed at Beamline X19C at National Synchrotron Light Source at Brookhaven National Laboratory, the small source dimension size (0.15mm × 0.35mm) and the long source-specimen distance contribute to the attainable spatial resolution of 4.2 μm when the specimen–film distance is 20cm. Diffracted images are recorded on Agfa Structurix D3-SC films. Exposure time depends on the actual geometry and recording media and it varies between a few seconds to a minute. Kodak D19 developer and fixer were used to process the exposed emulsions. The three types of x-ray topography geometries has been mentioned in chapter2, actually in this study, two types of SWXBT, transmission geometry and reflection geometry has been used for characterization of the studied samples.

Transmission geometry x-ray topography technique is shown in figure 3.1(a), film is placed behind the sample, incident and diffracted x-ray beams enter and exit from opposite sides of crystal. Due to x-ray beams in this geometry can pass thought the entire thickness of the crystal, so the record diffracted pattern contains the information in the entire sample, so relatively thick and low dislocation density samples can be characterized under this geometry. In order to get the certain reflection spot with the highest intensity, (001) plane, which is perpendicular to the crystal growth direction, is oriented perpendicular to the incident beam. The left side plane is (110), 220 topograph can be recorded by rotating 27^o about y-axis and is also verified by LauePt software. The entire sample can be covered by moving the sample stage up, down, left and right with the recording film at the same time. Figure 3.1(b) shows some topographs with different g vector using transmission geometry.

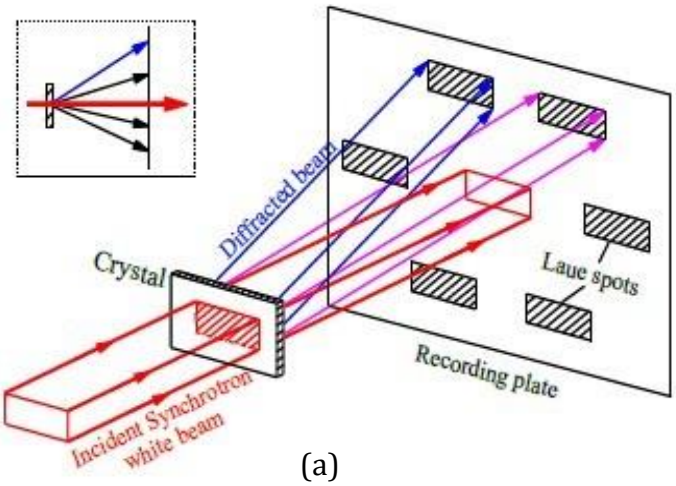

(a)

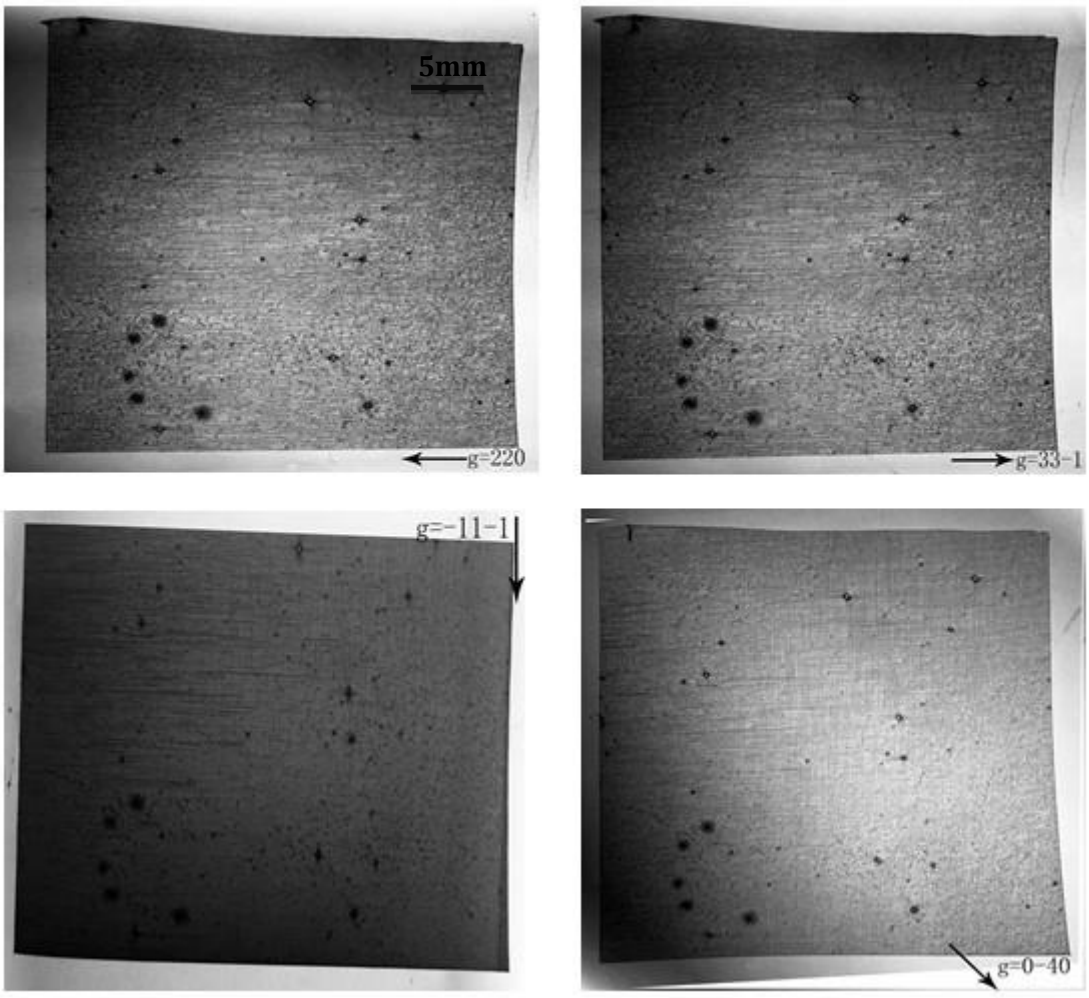

(b)

Figure 3.1. (a) Schematic of transmission x-ray topography technique, (b)Transmission topographs with different **g** vector 220, 33-1, -11-1 and 0-40.

Reflection geometry is shown in figure 3.2, and is the geometry when incident and diffracted x-ray beams enter and exit from the same side of crystals. This technique usually used for the crystals, which is too thick or contains high dislocation density ($>10^6/cm^{-2}$). As the X axis tilt angle increases, which means the angle between incident x-ray beam and normal vector of surface plane, the penetration depth increases. As a result, the diffracted pattern only contains the information near the surface of the sample. This geometry also can help to separate the defects information in epilayer from that in substrate.

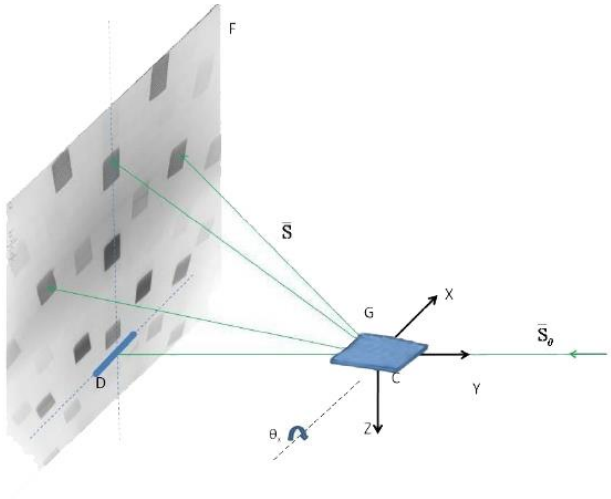

Figure 3.2. Schematic of reflection geometry x-ray topography technique.

3.3 High resolution x-ray diffraction

Double axis diffraction experiment was employed at SUNY at Stony Brook with the Bede D1system with Cu K_α target. As mentioned in the previous chapter, rocking curve width is the diffraction takes place over an angular range under the Bragg condition with given lattice plane and wavelength. Diffractometry involves the experimental recording of the rocking curve, such as diffracted intensity versus angle in the vicinity of a Bragg peak and measurement of the rocking curve width (FWHM). But in real radiation, the x-ray has both a wavelength spread and a divergence, in order to characterize high quality single crystal; multiple diffraction and angular-limiting apertures are used.

3.3.1 Double axis diffraction

Double axis diffraction is employed to get rocking curve widths in this experiment. Generally speaking, the double axis diffracometer (figure3.3) contains two axes, one is used for adjusting the beam conditioner and other to scan the sample through the Bragg angle. In order to monochromate and collimate divergent x-ray beams, multiple crystal arrangements have been used in high resolution x-ray diffractometer. The double axis rocking curve can be obtained by scanning the samples about the exact Bragg condition using small steps, in this experiment, 1arcsecond step has been used. Before scanning, specimen should be tilted to the optimial position, which means the specimen diffraction plane normal is in the dispersion

plane. Instrument adjustments can be achieved using control software installed in a computer which is connected to the instrument. After these settings, the detector axis is rotated to the twice the Bragg angle ($2\theta_b$), and the sample is rotated to the Bragg angle (θ_b). Then the sample is tilted by step of seconds to obtain the highest intensity and sharpest peak width. Then the $\theta - 2\theta$ rocking curves can be recorded with a narrow slit at the detector.

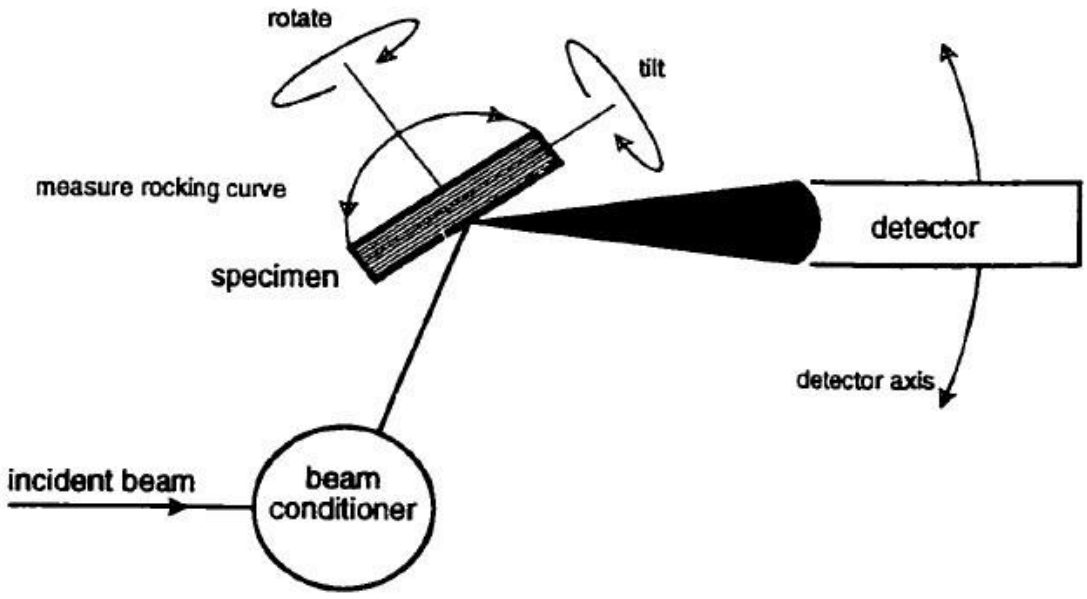

Figure 3.3. Double axis x-ray diffractometer

The rocking curve width can be influenced by tilts and strains in the crystals. Tilts can be caused by grains or sub-grains in the crystals and results in broadening the rocking curve or splitting the peak. Dilations are the region where the lattice planes are slightly different, it also can cause the rocking curve broadens or the peak splits. Additional information, such as substrate-epilayer mismatch, substrate offcut or layer tilt, layer thickness and epilayer composition can be deduced from the double axis rocking curves [27].

3.4 Growth method for silicon epilayer samples

Two samples were studied in this experiment. One is 60μm thick epitaxial film on a 720μm thick single crystal substrate. The epilayer is lightly boron doped with resistivity about 1 ohm-cm, and the substrate is heavily boron doped with resistivity about 0.015 ohm-cm. The other sample is free-standing 200μm thick epilayer film has the same doping level with the first one. The growth method for both two silicon epilayers is Chemical Vapor Deposition (CVD). CVD technique is often used to produce high-purity, high-performance thin films. The processing of this method is similar with LPCVD method that mentioned in chapter 1. It is based on the decomposition of silicon atoms which are generated from the chemical reaction of the silicon-containing source gas ($SiHCl_3$ or SiH_4) at the heated sample

surface. The carrier gas is high purity H_2, which also acts as a co-reactant. The free-standing 200μm thick epilayer film is separated from the silicon substrate using laser lift-off technique.

Chapter 4 Results

4.1 Defects in free-standing 200μm epitaxial single crystal silicon

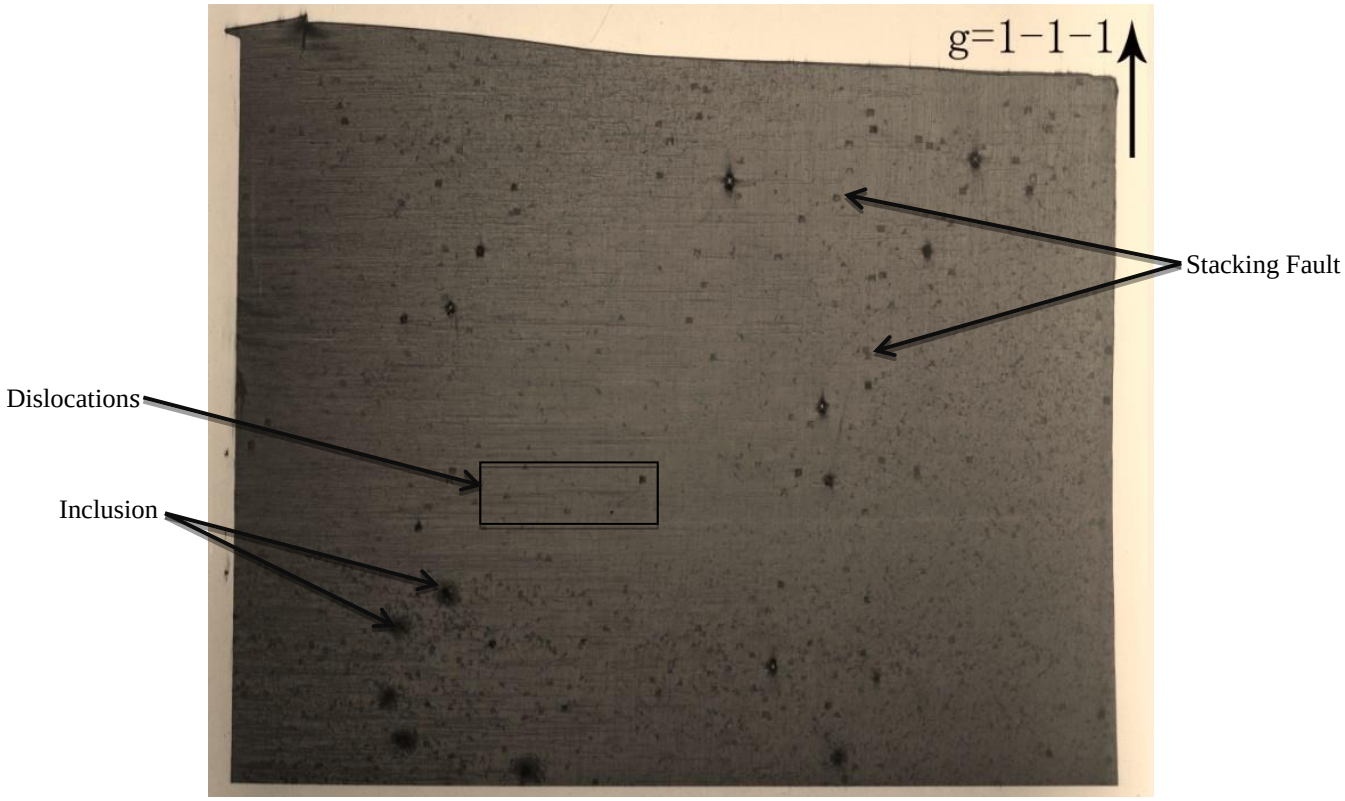

Figure 4.1. Defects in free-standing 200μm epitaxial single crystal silicon shown in 1-1-1 reflection.

4.1.1 Screw dislocations

Burgers vector ($\bar{\boldsymbol{b}}$) can be determined by contrast of dislocations from different topographs taken with different diffraction vector ($\bar{\boldsymbol{g}}$). $\mathbf{g} \cdot \mathbf{b} = 0$ is the criterion for invisibility of screw dislocations; $\mathbf{g} \cdot \mathbf{b} = 0$ and $\mathbf{g} \cdot \mathbf{b} \times \mathbf{l} = 0$ is the criterion for invisibility of edge or mixed dislocations. where **l** is the direction of dislocation line.

Figure 4.2 shows four transmission topographs recorded with different g vectors used for dislocation analysis. From the high magnification topographs with more detail shown in figure 4.3 we can observe that the dislocation lines which are aligned perpendicular along <1-1-1> direction are invisible in 1-1-1 and -220 refelctions, while those dislocations are visible in 220 reflection. Based on the $\mathbf{g} \cdot \mathbf{b}$ criterion, those dislocations are parallel to Burgers vector and we can confirm they are screw dislocations with Burgers vector 1/2[110]. In addition, dislocations perpendicular to <220> direction are invisible in 220 (figure4.3 b) and visible in <1-1-1>, which are also parallel to burgers vector, and they are screw dislocations according to the $\mathbf{g} \cdot \mathbf{b}$ criterion. But the Burgers vectors possibility can be both 1/2[1-10] or 1/3[1-11]. These

dislocations are invisible in 33-1 (figure4.3.d), and in order to satisfy the $\mathbf{g} \cdot \mathbf{b} = 0$ criterion, Burgers vector can only be 1/2[1-10].

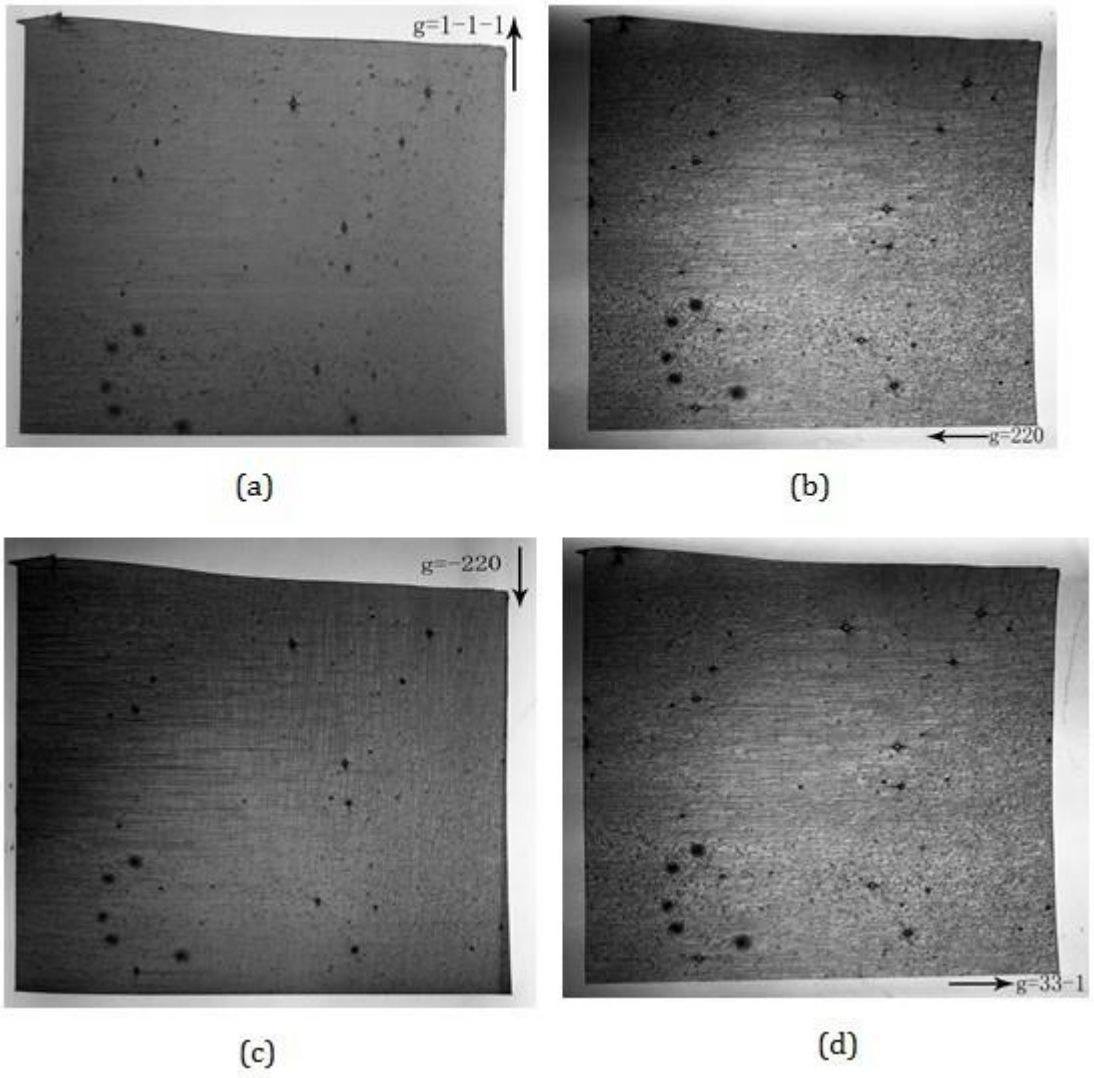

Figure 4.2. Transmission topographs from free-standing 200μm epitaxial single crystal silicon. (a)g= 1-1-1; (b)g= 220; (c) g=-220; (d) g=33-1.

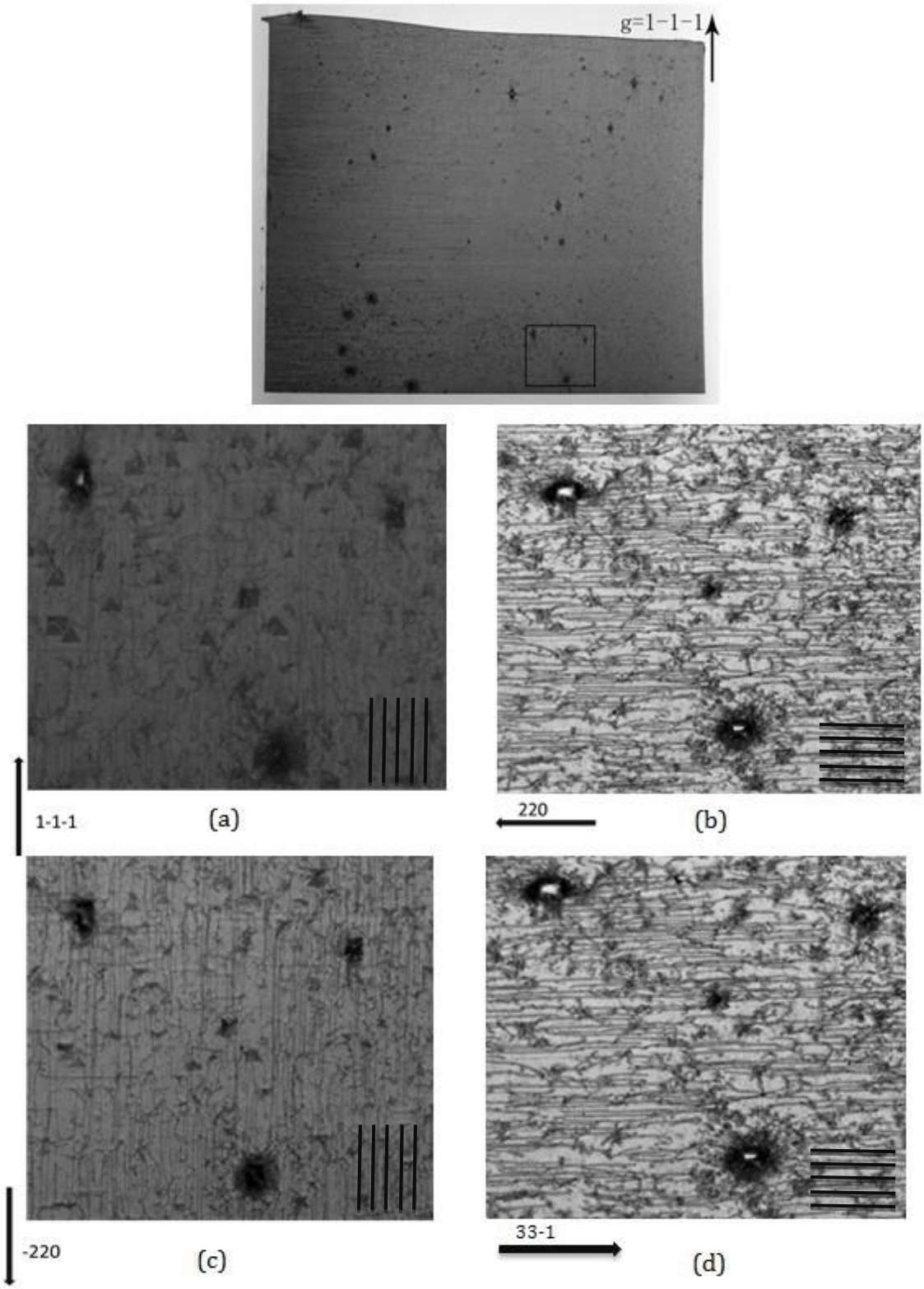

Figure 4.3. High magnification topographs from selected region of different reflections. Some inclusions are observed in these images. (a) g=1-1-1; (b) g=220; (c) g=-220; (d) g=33-1. The black parallel lines show the dislocation direction in these topographs.

4.1.2Misfit Dislocations

Many misfit dislocation arrays are observed in transmission topographs as shown in figure 4.3. Misfit dislocations, also called interfacial dislocations are easily observed in the lattice-mismatched epitaxial layers. The critical thickness is defined as the thickness at which the first misfit dislocation nucleates. In this sample, the substrate and epitaxial layer have the same lattice structure of silicon, but with different doping level, so misfit dislocation can be observed due to the different lattice constant. Relaxation mechanism for lattice-mismatched epilayers has been proposed by Matthews and Blakeslee in 1970s. In this mechanism, threading dislocations are bowed to form misfit dislocation segments due to the misfit stress, the critical thickness can be determined by the force acting on the dislocations. The main two forces are F_ε the force exerted by the misfit strain, and F_l the tension in the dislocation lines.

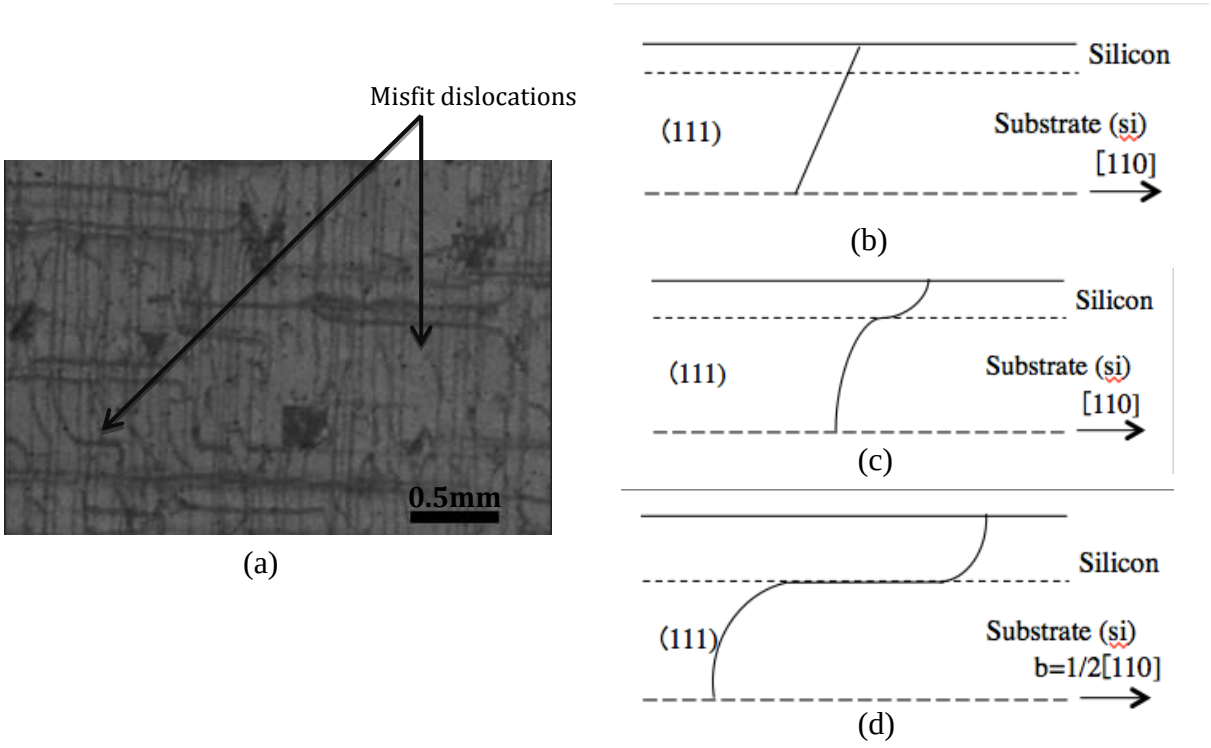

Figure 4.4. (a) Magnification image with area contains misfit dislocations in -11-1 reflection. (b), (c), (d) illustrate the mechanism for formation of misfit dislocations with burgers vector 1/2[110], which has been analyzed in 4.1.1, and the it is screw dislocation.

The mechanism for formation of misfit dislocations is illustrated in figure 4.4.(b) shows a dislocation line in (111) plane with a burgers vector ½(110) extends from substrate layer to the epitaxial layer, in where $F_\varepsilon < 2F_l$. In figure 4.3.(c), where $F_\varepsilon = 2F_l$, the threading dislocation becomes bowed. When $F_\varepsilon > 2F_l$, it will cause the dislocation to glide to the right as shown in figure 4.4.(d). If the layers are isotropic and have the same elastic constants, then

$$F_\varepsilon = \frac{2G(1+\upsilon)}{(1-\upsilon)} bh\varepsilon \cos\lambda$$

And

$$F_l = \frac{Gb^2}{4\pi(1-\nu)}(1 - \upsilon\, cos^2\alpha)(\ln\frac{h}{b} + 1)$$

Where G is the shear modulus of layers, ν is the Poisson's ratio, b is the Burgers vector, H is the epitaxial layer thickness, ε is the misfit strain, α is the angle between the burgers vector and the dislocation line and the λ is the angle between the slip direction and direction in the film plane that is perpendicular to the line of intersection of the slip plane and the sample surface.

The thickness at which $F_\varepsilon = 2F_l$ is defined as the critical thickness, H_c, is given b

$$H_c = \frac{b}{4\pi f}\frac{(1-\nu\cos^2\alpha)}{(1+\nu)\cos\lambda}(\ln\frac{H_c}{b} + 1)$$

Where f is the misfit strain.

The half-loops like misfit dislocations have been observed in these dislocations as shown in figure 4.5 (a). The mechanism of this type dislocation is two threading dislocations glide with opposite Burgers vectors and the misfit dislocations they produced annihilate one another as shown in figure 4.5 (b) [28] [29] [30].

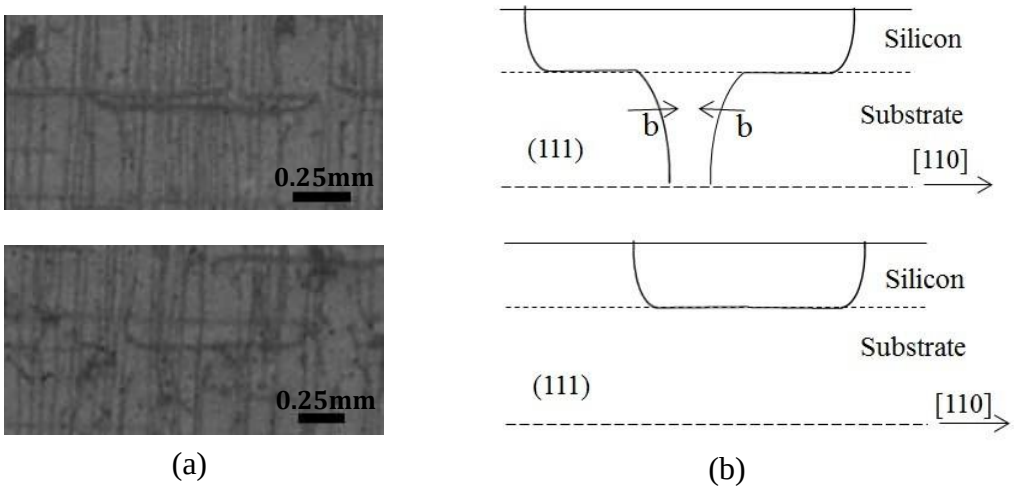

(a) (b)

Figure 4.5. (a) Magnification image contains half-loop like misfit dislocation in -11-1 reflection, (b) Formation mechanism of half-loop like dislocation.

4.1.3 Stacking fault

In diamond FCC structure, the close-packed planes are {111} planes, as we mentioned in the chapter 1, the stacking sequence is ABCABCABC…most of the stacking fault occurs in the slip planes, which are classified as intrinsic or extrinsic, as suggested by Frank [31]. The intrinsic stacking fault is formed when a layer of plane is removed from the original stacking sequence, giving

ABCABC BCABC

The extrinsic stacking fault is formed when a layer of atoms is inserted at the normal sequence, giving

ABCABCBABCABC

From the transmission topographs, an interesting stacking fault feature has been observed; the square feature is shown in figure 4.6. The square feature presents different shapes in different reflections. In 1-11 (figure 4.6.c), a rectangle shape feature can be observed which contains a white line triangle; in 2-20 (figure 4.6.d), they are two combined triangles; and the perfect square feature are shown in the 040 reflection (figure 4.6.e). The stacking fault on four (111) faces consists of a pyramid structure which shown in figure 4.6.c, thus the stacking fault features are the projection of the pyramid structure on plane (1-11), (2-20), (040). In order to prove this hypothesis, a set of images (figure 4.7.) were taken by optical microscopy from surface plane (001). The images give the information for mechanical formation of these stacking faults.

The contrast from stacking faults in x-ray topography arises from the phase shift experienced by the x-ray wavefields as the cross the fault plane:

$$\delta=(-2\pi\, g\cdot R)$$

Where g is the active reciprocal lattice vector for the reflection and R is the fault vector. Contrast is expected to:
disappear when $\delta = 0$ (corresponding to g.R=integer);
be very weak when $\delta = \pm\pi/6$ (corresponding to g.R=±1/12, ±11/12);
be weak but visible for $\delta = \pm\pi/3$ (corresponding to g.R=±1/6, ±5/6);
be very well marked for $\delta = \pm\pi/2$ and $\pm 2\pi/3$ (corresponding to g.R=±1/4 ±3/4, ±2/3 and ±1/3) [32] [33].

The triangle feature is invisible in 1-1-1 reflection (figure 4.8.a) and visible in 1-11, -220 reflections. Concluding from the stacking fault contrast analysis, the stacking fault is the Shockley fault with R = 1/6 [1-12]. If the B plane and all planes above it are displaced by the vector 1/6 [211], the B plane moves into a C position, and the planes above it undergo the transition A -> B, B -> C, and C -> A, relative to positions fixed on the original A plane. This shear displacement is represented by the arrows in the reaction

ABCABCABCABC

CABCABCA [34]

Table 1.

g	1-1-1	1-11	-220
g.R	0	2/3	-2/3

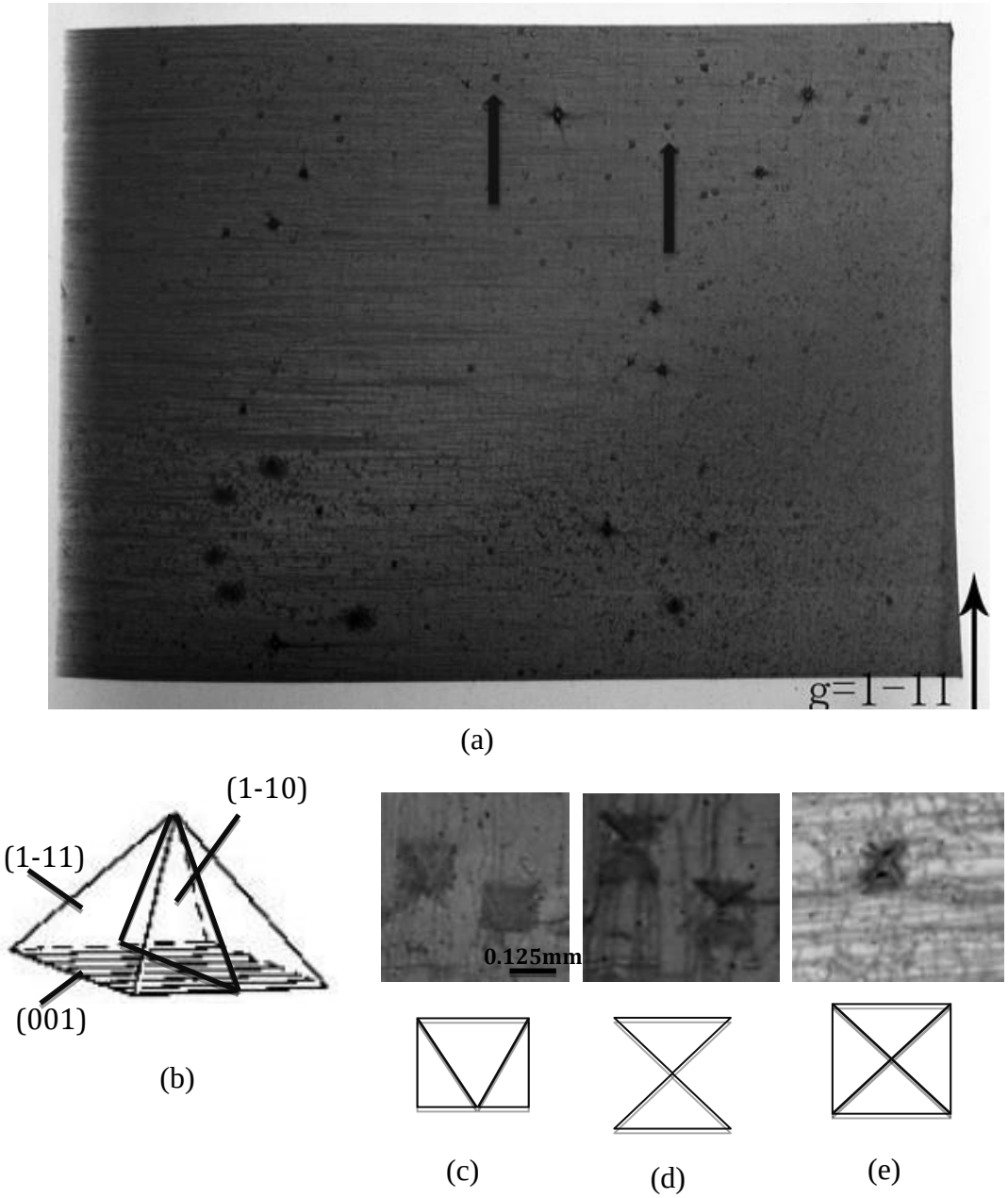

(a)

(b)

(c)

(d)

(e)

Figure4.6. (a) Transmission topography of 1-11 reflection; (b) the pyramid structure, up four faces are formed by (111) and bottom face a (001); (c) square feature in 1-11 reflection; (d) square feature in 2-20 reflection; (e) square feature in 040 reflection.

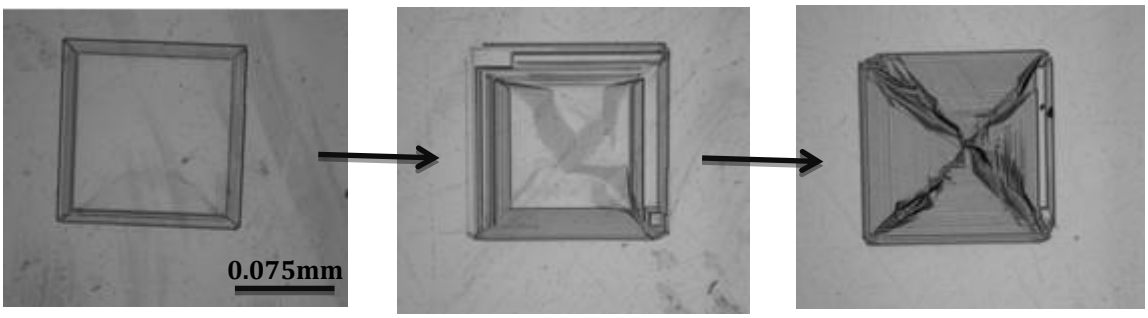

Figure 4.7. Images from optical microscopy on surface plane (001) in BF mode shows mechanical formation of stacking fault

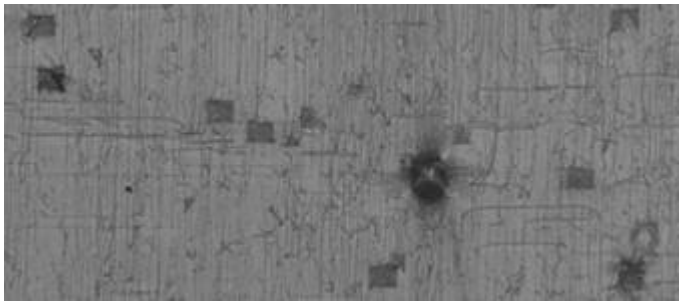

(a)

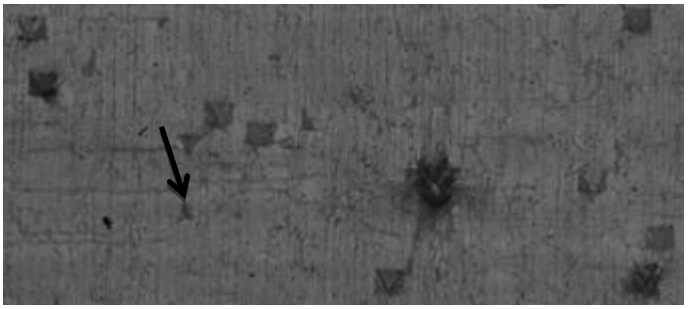

(b)

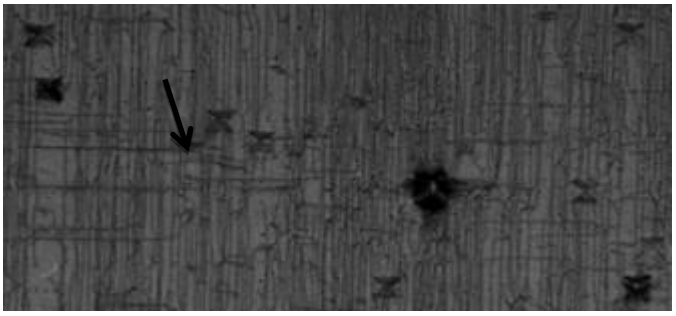

(c)

Figure 4.8. The triangle dark feature is invisible in (a) and visible in (b) and (c), the reflection of these three topography are separately 1-1-1, 1-11, -220.

4.2 Silicon epitaxial (~60µm) with the silicon substrate (~720 µm)

Figure 4.9 shows the 004 reflection topograph of the 60µm thickness silicon epitaxial with the silicon substrate.

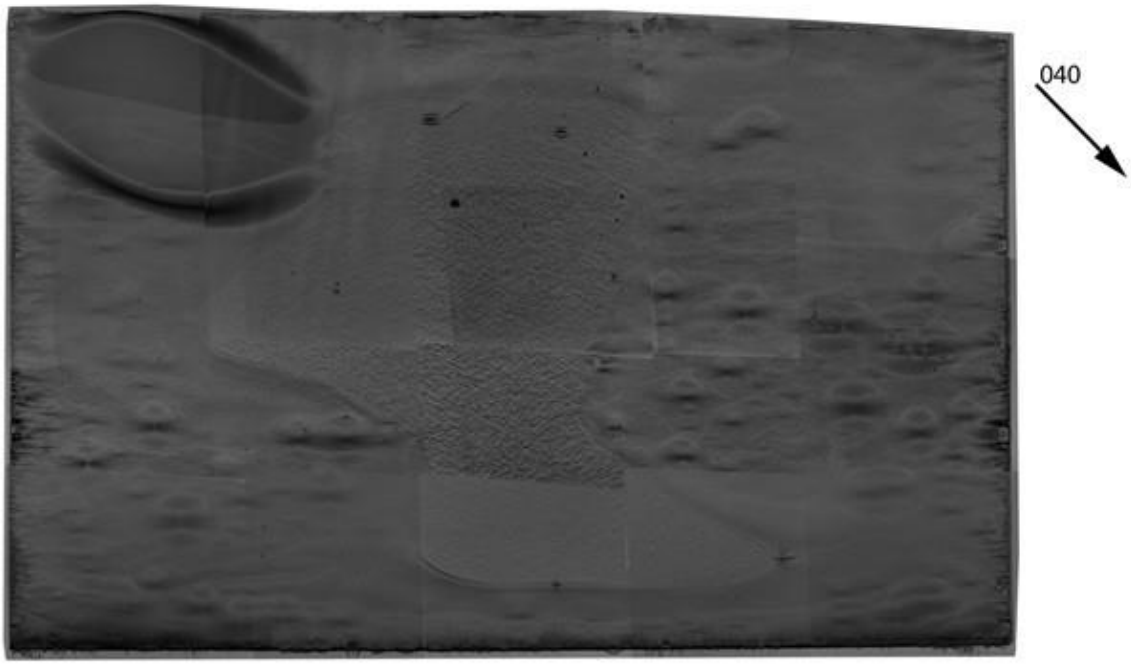

Figure 4.9. Reflection topography (**g** = 040) of 60µm thickness silicon epitaxial with the silicon substrate.

4.2.1 Threading dislocation

Figure 4.11 shows x-ray topographs which are taken using monochromatic x-ray source at the Advanced Photon Source (APS) from the middle section of this sample. The schematic setting at APS is illustrated in Figure 4.10. Appropriate wavelength is set to satisfy the Bragg condition by rotating the monochromater. The white beam in APS is monochromatized by two parallel Si(111) crystals and the x-ray energy is tunable between 2.4 – 40 keV.

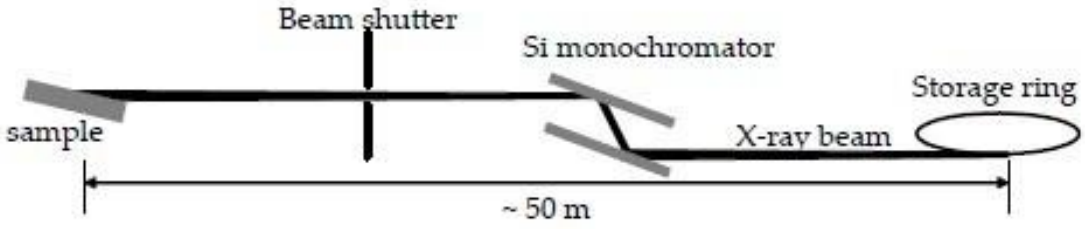

Figure 4.10. Schematic showing the experimental setting-ups at APS.

The region on the sample is highlighted with white squares in figure4.11(a). Many threading dislocations are observed in this figure as white dots, and the area containing threading dislocation is magnified in figure 4.11(b). Threading dislocation lines usually parallel or almost parallel to the growth direction, the growth direction in silicon is <001> and the threading dislocation lines glide on (111) planes as figure 4.12. Misfit dislocation is the origin for threading dislocation in silicon; hence dislocations cannot end inside the crystal so they need to end in another dislocation, at a surface or on an impurity. For the misfit dislocation segment which is entirely inside the crystal there will always be a threading dislocation at the two ends of the misfit dislocation that thread to the surface. The mechanism for half-loop misfit dislocation with two TD is shown in Fig 4.1.3. Acting on this half-loop will let it glide to the direction of surface on (111) plane. As a result, the misfit dislocation segment can't be observed connect with white dots in 040 reflection.

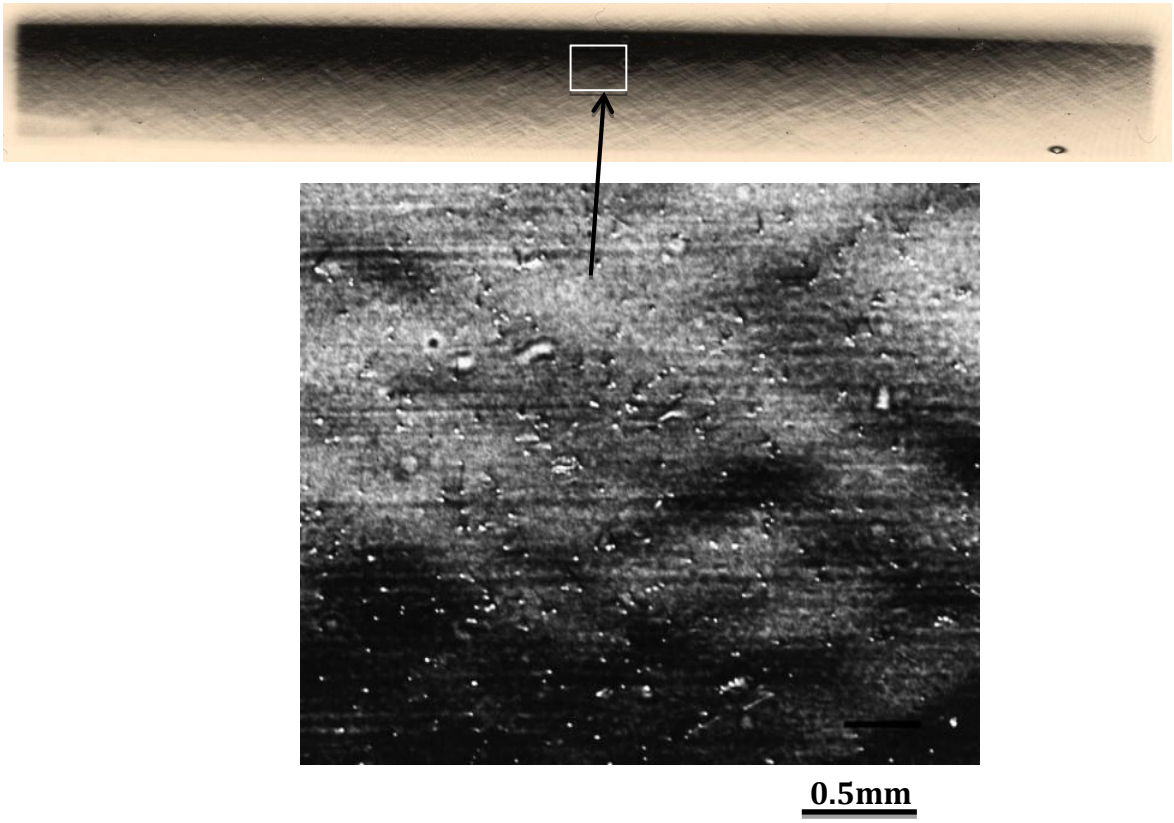

Figure 4.11. Reflection topography from APS with 040 reflection. (a) image from middle section of the sample, (B) magnification images from the area of the white square in (a).

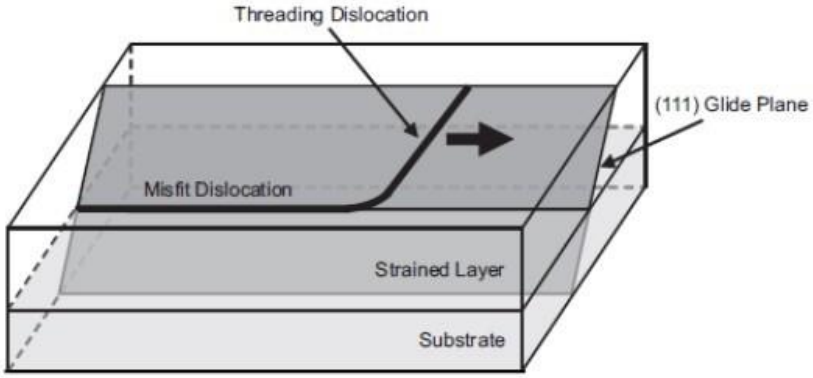

Figure 4.12. Illustration for the formation of TD

In addition, some diamond shape features are observed as shown in figure 4.13. Four separate white lines compose these diamond shapes. Some of these segments are accompanied with white dot at the end of each segment. These white lines are misfit dislocations lying on the interface between substrate and epilayer, and aligning along the intersection of (111) and (001) [35].

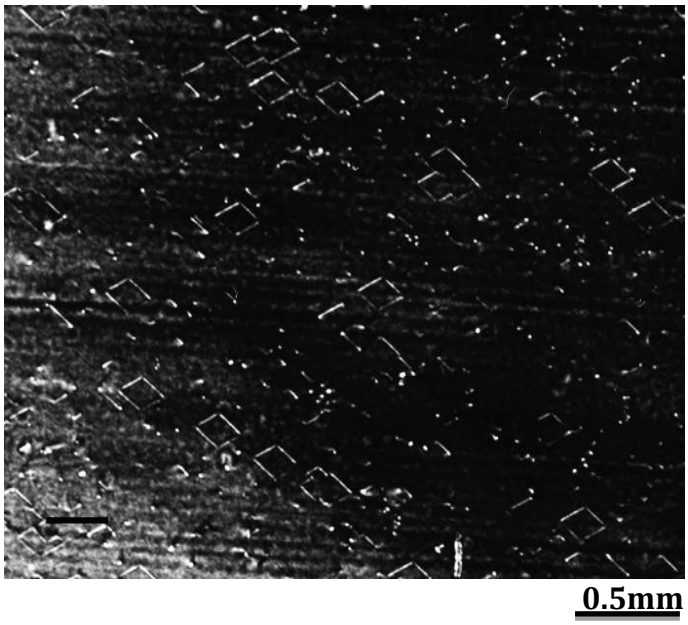

Figure 4.13. Diamond shape misfit dislocations represented in the magnification image.

4.2.2 Strains in silicon epitaxial

Strains in silicon epitaxial are mainly caused by mismatch between epilayer and substrate during the processing of crystal. Avoiding strain generation during growth and processing is a critical problem in solar cell industry, due to its effect on the efficiency of solar cells.

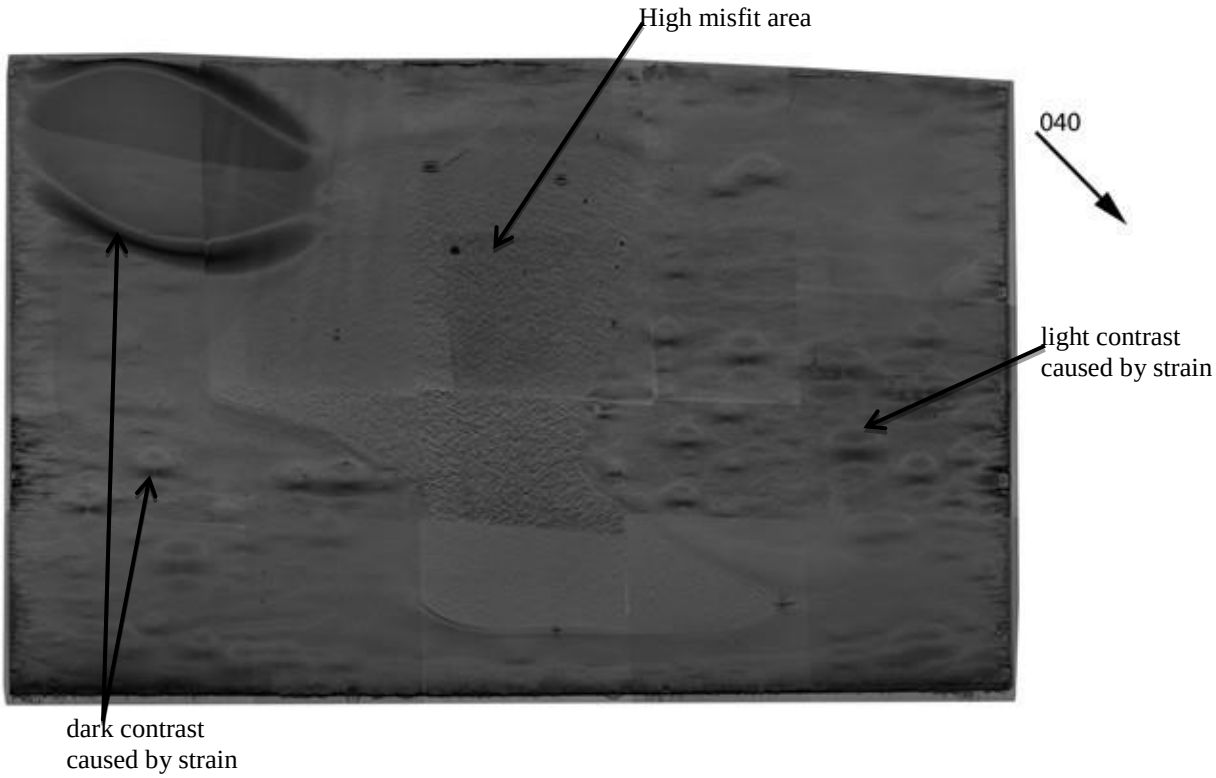

Figure4.14. Transmission topograph shows strain area and strain free area.

As figure 4.14 shows, some areas have relatively dark or light contrast due to the orientation contrast. This contrast has been described in chapter 2. Strains cause the misorientation in this silicon sample, and convergence and separate of x-ray beam is the main reason for dark or light contrast. It is assumed that image distortion is generated from the strain region.

In order to prove the distortion is caused by strain, section topography combined with HRXRD is used for analysis.

Among XRT techniques, section topography is the most fundamental. Figure4.15 (a) shows the geometry for section topography. In section topography, a narrow x-ray beam is incident on the sample through an extremely narrow slit (~10μm), diffraction from a restricted volume is taken. On this topograph, fringes are visible in a perfect crystal. The advantages of section topography is very small lattice strains can be observed because they distort the fringes, and defects can be located as a function of depth in the crystal which is dominated by direct image contrast [36] [37]. Figure 4.15 (b) shows the section topograph taken from the upper left strained region of sample and the three shots of the section topographs by moving sample 50μm at each time.

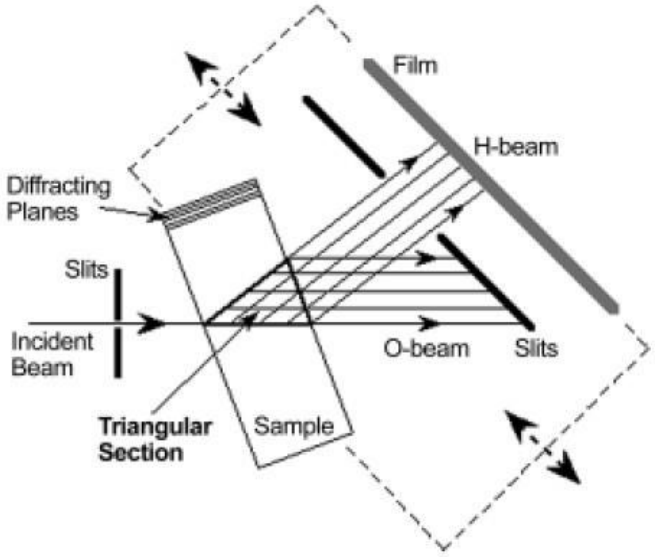

(a)

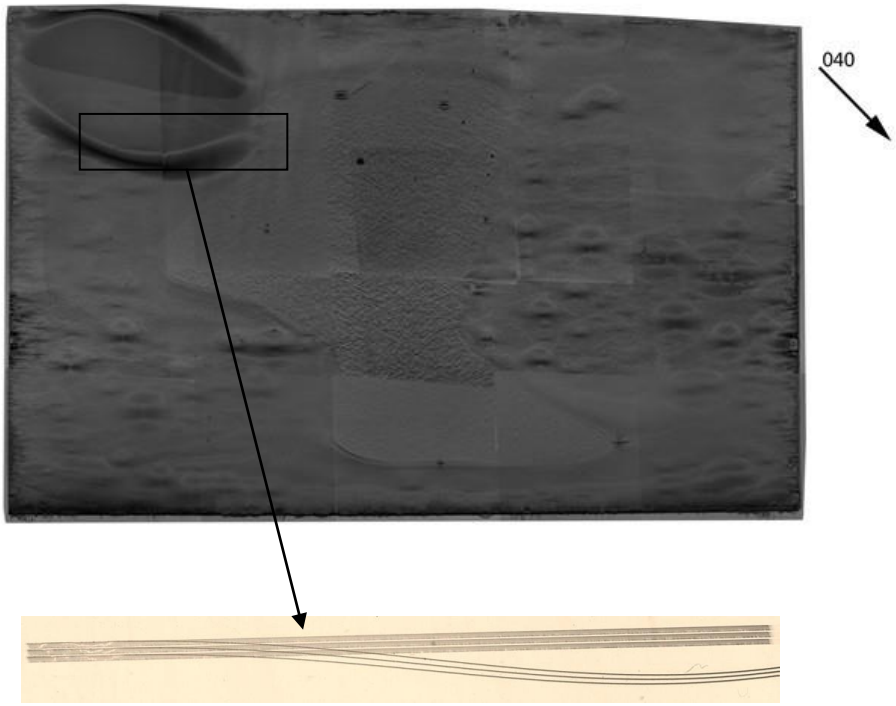

(b)

Figure4.15. (a) The geometry for section topography, the transmitted diffraction image from a restricted region is recorded, (b) section topograph from high strain area.

HRXRD technique has been mentioned in chapter 3. Double axis x-ray diffraction is employed in this experiment. Rocking curve with 121 different positions on the crystal have been recorded with the rotation ranging from -450 – 450 arcsec and steps of 1arcsec. Figure 4.16 is one of the rocking curves we recorded with a narrow rocking curve width.

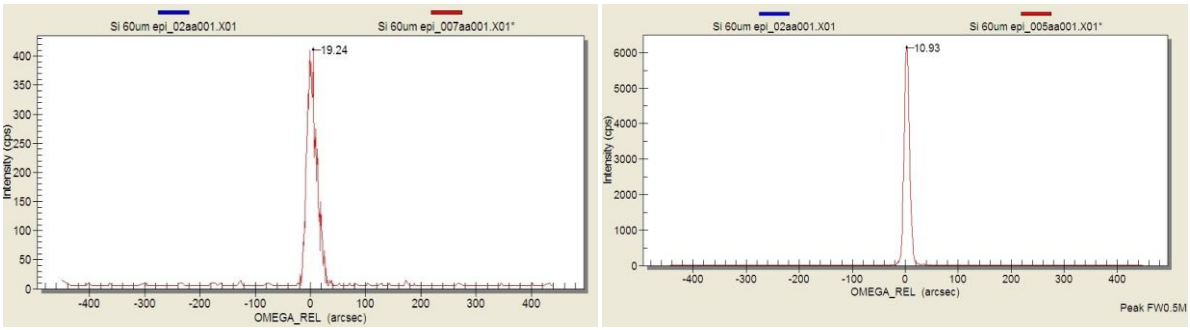

(a) (b)

Figure 4.16. (a) Typical 004 rocking curve recorded from epitaxial silicon on substrate (FWHM = 19.24”); (b) 004 rocking curve for perfect silicon crystal (FWHM = 10.93”)

The rocking curve for totally 121 positions is recorded as shown in figure4.17.The value for rocking curve widths is listed in table 2.

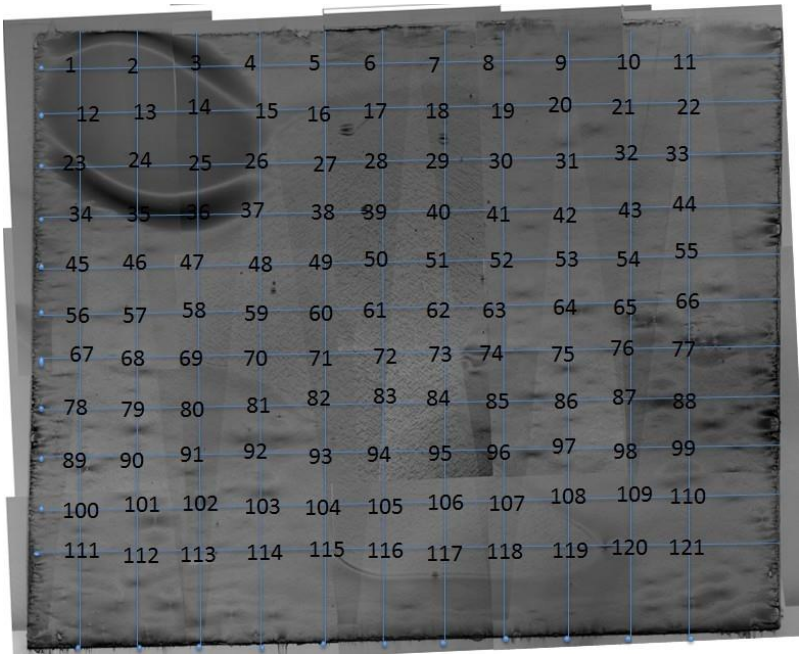

Figure 4.17. 121 positions on the epitaxial silicon layer from which rocking curves have been recorded as shown in Table 2.

Table 2. The rocking curve widths of 121 positions.

Y / X	1	2	3	4	5	6	7	8	9	10	11
1	436	234	164	130	207	194	13.6	51.6	146	413	191
2	160.8	(1)	25.6	19.7	23.5	21.7	51.1	242	12.5	(2)	17.7
3	37.5	17.3	32.5	12.3	11.3	12.4	53.8	16.6	58.9	19.1	22.8
4	212	193	63	161	164	164	17.1	26	30	36.8	18.2
5	273	376	251	208	184	172	36.7	15.7	73.5	119	118
6	215	35.6	35.1	28.7	37	38.3	18.8	14.1	(3)	77.2	88.9
7	43	32.5	31.9	31.8	33	34.5	49.6	37.2	66.7	69.2	(4)
8	62.4	29.6	45.1	48.9	34.4	36.1	42.2	54	26.6	(5)	45.6
9	52.3	64.6	18.7	26.5	32.1	32.2	48.5	45.4	45.2	39.6	44.7
10	40.7	185	106	(6)	163	179	45	(7)	45.5	52.4	66
11	286	833	235	209	192	173	28	38.4	51.5	56	37

Two peaks are present in the positions which are blank in Table 2. Figure 4.18. is the 3D model generated by Matlab software illustrates the distribution of FWHM in this sample without the two peaks position value.

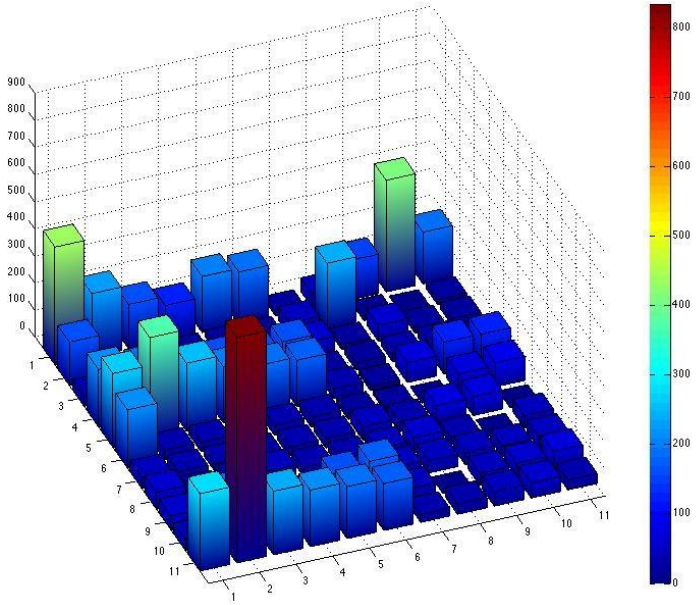

Figure 4.18. 3-D model for FWHM distribution, X axis stands for horizontal length of this sample, and Y axis stands for the vertical length of this sample and Z axis stands for the FWHM value.

From the figure we observe that in the middle of this sample the FWHM is relatively low, which is the strain free region where dislocations are formed to relax the strain; FWHM near the four edges of this silicon sample is relatively high, especially in the upper left corner, the area which has apparent dark and light contrast with high FWHM value. The FWHM value has a good match with the information given by transmission topography.

In Chapter 2, the equation for penetration depth was given by:

$$t = \frac{1}{\mu(\mathrm{cosec}\alpha+\mathrm{cosec}\beta)}$$

Where μ is the mass absorption coefficient which is a function of wavelength λ:
$\mu = -0.1508\lambda^6+1.3684\lambda^5-7.2723\lambda^4+50.179\lambda^3-6.6116\lambda^2+2.775\lambda-0.0166$ [20]

Here the wavelength of CuK_α is 1.54056Å. α and β are the entrance and exit angle between the crystal surface and beam and equal to 35.1 degree. After the calculation, the penetration depth t is 2.34μm. Since the thickness of the silicon epilayer is 60μm, the rocking curves are unlikely to contain any contribution from the substrate.

Chapter 5 Conclusion

The main work in my study is focused on characterizing the defects in 60μm thickness single crystal silicon epilayers with 720μm silicon substrate and 200μm single crystal silicon free standing epilayer using SWBXT, monochromated X-ray topography, optical microscopy and double axis x-ray diffraction techniques. The defects structure and formation mechanisms are discussed in detail.

1) In 200μm single crystal silicon epilayer, linear and planar defects are studied. For dislocations, the dislocation density is $9.4\times 10^{3}cm^{-2}$, arrays of screw dislocations with Burgers vector 1/2<110> and 1/2<1-10> has been determined based on the $g \cdot b$ criterion. Misfit dislocations, also of screw type, are formed by the bowing of threading dislocations which are gliding on the (111) planes under misfit stress. Square-shaped stacking faults are also observed on 004 reflections which contain stacking faults in four neighboring (111) planes resulting in a pyramid structure. Different stacking fault morphologies are due to the projection of this pyramid structure.

2) In 60μm thick single crystal silicon epilayer with 720μm silicon substrate, threading dislocations (TDs) and misfit dislocations are concentrated in the middle area, and the area, which contains strains are concentrated near the four edges of the sample. TDs are generated from the two ends of the misfit dislocations. The strain distribution is also revealed by the significant distortion of epilayer in section topographs and also the broadening of the FWHM of rocking curves recorded from these regions. These are consistent with the observations on the SWBXT topographs.

References:

[1] E. Lorenzo, Soalr Electricity: Engineering of Photovoltaci Systems., Progensa: ISBN 84-86505-55-0, 1994.

[2] [Online]. Available: http://en.wikipedia.org/wiki/File:Pn-junction-equilibrium.png.

[3] K. R. Michelle J. McCann, "A Review of Thin Film Crystalline Silicon for Solar Cell Applications. Part 1: Native Substrates,," *Solar Energy Materials & Solar Cells ,* vol. 68, no. 135, 2001.

[4] R. C. A. Slaoui, "Advanced Inorganic Materials For photovoltaics," in *MRS Bulletin*, 2007.

[5] [Online]. Available: http://en.wikipedia.org/wiki/Solar_cell.

[6] [Online]. Available: http://www.green-planet-solar-energy.com/solar-energy-cell-crystals.html.

[7] [Online]. Available: http://people.seas.harvard.edu/~jones/es154/lectures/lecture_2/materials/materials.html.

[8] W. O Mara, Oxygen, Carbon and Nitrogen in Silicon, Park Ridge, NJ, USA: Noyes Publications, 1990.

[9] Z. Li et al., *IEEE Trans Nucl. Sci.,* vol. 39 (6), no. 1730, 1992.

[10] [Online]. Available: http://www.jhaj.net/jasjeet/tcad/Learn1/l1k.htm.

[11] [Online]. Available: https://en.wikipedia.org/wiki/Float-zone_silicon.

[12] R. Brown and Z. M. T. Wang, "Engineering Analysis of Microdefect Formation During Silicon Crystal growth," *Journal of Crystal Growth,,* pp. p97-109, 2001.

[13] A. K. W. K. a. B. M. A Stoffel, "LPCVD against PECVD for Micromechanical Applications,," *J. Micromech. Microeng.,,* vol. 6, no. 1, pp. p. 20-33, 1996.

[14] [Online]. Available: http://www.dowcorning.com/content/etronics/etronicschem/etronics_newcvd_tutorial3.asp.

[15] D. C. Harris, "A century of sapphire crystal growth: origin of the EFG method," *SPIE Proceedings,* vol. 7425, 2009.

[16] C. M. R. S. S. H.J. Moller, *Thin Sol. Films 487,,* p. 179, 2005.

[17] J. H.E. LaBelle, *Nature,* p. PP.574, 1967.

[18] i. K. J. W. S. (. H.J. Moller, "Handbook of Semiconductor Technology - Electronic Structure and Properties of Semiconductors,," Weinheim, Germany,, Wiley-VCH, 2000, p. pp. 715.

[19] H. al., *Thin Solid Films 487,* pp. p. 179-187, 2005.

[20] Vishwanath Sarkar, "Defect characterization and stress analysis by white beam synchrotron X-ray topography,," p. p. 27, 2011.

[21] Y. Chen, "Defects Structure in Silicon Carbide, Bulk Crystals, Epilayers and Devices," p. p. 45, 2008.

[22] G. D. J. B. M. D. Balaji Raghothamachar, "Defect Analysis in Crystals Using X-ray Topography,," *Microscopy Research and Technique 69,* pp. p. 343-358, 2006.

[23] Chen Yi, "Defects Structures in Silicon Carbide, Bulk Crystals, Epilayers and Devices," p. p. 10, 2008.

[24] B. Raghothamachar, "Synchrotron White Beam X-ray Characterization of Growth Defects in Bulk Compound Semiconductor," p. p. 98, 2001.

[25] A. Authier, in *Dynamical Theory of X-tay Diffraction*, Oxford University Press, 2001, p. p. 85.

[26] D Hull and D J Bacon, in *Introduction to Dislocations,*, p. p. 82.

[27] B. Raghothamachar, "Synchrotron White Beam X-ray Characterization of Growth Defects in Bulk Compound Semiconductor," p. p. 68, 2001.

[28] Matthews J W and Blakeslee A E, *J. Cryst. Growth 27118,* 1974.

[29] M. S. a. L. T. Matthews J W, *Appl. Phys.41 ,* p. 3800, 1970.

[30] M. J. W, *J. Vac. Sco. Technol,* p. 12 126, 1975.

[31] F. C. Frank, *Phil. Mag.,* pp. 42, 809, 1951.

[32] Authier and Y. Epelboin, *Phys. Stat. Sol.,* pp. 41, K9, 1977.

[33] F. W. H. W. S. B. B. R. G. C. S. S. M. Dudley, "Stacking Faults Created by the Combined Deflection of Threading Dislocations of Burgers Vector c and c+a During the Physical Vapor Transport Growth of 4H–SiC,," *Applied Physics Letters,,* vol. 98, no. 1, 2011.

[34] J. P. Hirth, in *Theory of Dislocations,*, 1930, p. p. 306.

[35] S. G. a. L. S. J. E. Ayers, "Threading Dislocation Densities in Mismatched Heteroepitaxial (001) Semiconductors," in *MRS Proceedings*, 1991.

[36] G. G. L. David R. Black, "X-Ray Topography," p. p. 7.

[37] F. S. S. S. B. R. M. D. H. Wang, "Combined Application of Section and Projection Topography to Defect Analysis in PVT Grown 4H-SiC," in *Mater. Res. Soc. Symp. Proc. Vol. 1433*, 2012.

[38] H. al., *Thin solid Films 487,* pp. pp.179-187, 2005.

[39] [Online]. Available: http://www1.chm.colostate.edu/Files/HRXRD.pdf.

[40] [Online]. Available: http://people.seas.harvard.edu/~jones/es154/lectures/lecture_2/materials/materials.html.

[41] [Online]. Available: http://people.seas.harvard.edu/~jones/es154/lectures/lecture_2/materials/materials.html.

[42] S. Bau, "High-temperature CVD silicon films for crystalline silicon thin-film solar cells," pp. p 9-30, 2003.